

Halo Photometry and Asteroseismology for 98 of the Brightest Stars Observed by TESS

Jonatan Rudrasingam¹,^{*} Timothy R. Bedding¹, Benjamin J. S. Pope², May Gade Pedersen¹,
Mikkel N. Lund³, Timothy R. White⁴, and Daniel Hey⁵

¹*Sydney Institute for Astronomy, School of Physics, University of Sydney, Sydney, NSW 2006, Australia*

²*School of Mathematical and Physical Sciences, Macquarie University, 12 Wally's Walk, Macquarie Park, NSW 2113, Australia*

³*Stellar Astrophysics Centre, Department of Physics and Astronomy, Aarhus University, Ny Munkegade 120, DK-8000 Aarhus C, Denmark*

⁴*Sydney Informatics Hub, Core Research Facilities, University of Sydney, NSW 2006, Australia*

⁵*Institute for Astronomy, University of Hawai'i, 2680 Woodlawn Drive, Honolulu, HI 96822, USA*

Accepted 2026 February 24. Received 2026 February 23; in original form 2026 January 22

ABSTRACT

The Transiting Exoplanet Survey Satellite (TESS) mission has facilitated studies of asteroseismology, eclipsing binaries, and transits in many stars. However, the brightest stars saturate TESS, yet they are the most amenable to photon-hungry high-resolution studies and have long observational histories. In this work, we adapted the halo photometry used in *K2* to extract light curves from the unsaturated halo pixels of the star's point spread function. We used this method to extract light curves for 98 of the brightest stars observed by TESS in Sectors 1–93. These bright stars include 15 red giants, five δ Scuti variables, eight stochastic low-frequency variables, eight eclipsing binaries, and 46 other variables. We measured ν_{\max} for 13 red giants using *pyMON* and $\Delta\nu$ for one of them, β Gem (Pollux). For five of them, this represents the first time that oscillations were detected. We derived their stellar masses using the measured ν_{\max} and previous interferometric and radiometric angular diameters. We also discovered δ Scuti and γ Doradus variability in α Cep, possible asteroseismic binary signatures in ϵ Car, and a new eclipsing binary, γ And. Furthermore, we identified 18 stars in our sample that will be observed by the future PLAnetary Transits and Oscillations of stars (PLATO) mission, and 69 stars that have Stellar Observations Network Group (SONG) observations, including some simultaneous with TESS. The light curves are publicly available on the Mikulski Archive for Space Telescopes.

Key words: asteroseismology – stars: binaries: eclipsing – stars: oscillations – stars: variables: general – techniques: photometric

1 INTRODUCTION

The Transiting Exoplanet Survey Satellite (TESS), launched in 2018, has now observed nearly the entire sky, providing high-precision photometry for many bright, nearby stars (Ricker et al. 2014, 2015). This has allowed many studies of oscillating stars, eclipsing binaries, and planetary transits (see review by Winn 2024). For some regions in the sky, TESS has now provided longer time series than *Kepler*. However, the TESS detector begins to saturate around seventh magnitude and electrons bleed into neighbouring pixels. Depending on the magnitude, the star can produce long bleed columns. Although studies have been made using TESS photometry for solar-like oscillators up to at least second magnitude (e.g. Lund et al. 2025), and O/B and A/F stars up to zeroth magnitude (e.g. Pedersen et al. 2019; Antoci et al. 2019; Bowman et al. 2022; Sharma et al. 2022; Rieutord et al. 2024), there are no systematic studies dealing with all the brightest stars observed by TESS.

Bright stars are important because it is possible to do complementary observations including: interferometry (e.g. Baines et al. 2023); spectroscopy (e.g. Strassmeier et al. 2018); spectropolarimetry (e.g. Zwintz et al. 2020); long-term radial-velocity (RV) monitoring of

stellar companions, exoplanets, or unknown stellar variability (e.g. Hatzes et al. 2018); and ground-based asteroseismic observations, either simultaneously (e.g. Kjeldsen et al. 2025) or otherwise (e.g. Arentoft et al. 2019; Knudstrup et al. 2023). Furthermore, some of these stars have been observed by other space-based missions such as the 52-mm star camera on Wide Field Infrared Explorer (WIRE; Buzasi 2000; Buzasi et al. 2000), the Solar Mass Ejection Imager on the Coriolis satellite (SMEI; Jackson et al. 2004), the Microvariability and Oscillation of Stars (MOST; Walker et al. 2003), and the BRiGht Target Explorer (BRITE)-Constellation (Weiss et al. 2014; Pablo et al. 2016). Obtaining TESS photometry can help validate and improve previous results from these missions.

For *Kepler* and *K2*, different methods have been developed to deal with saturated stars. One of these, smear photometry (Pope et al. 2016, 2019a), uses collateral smear measurements to obtain the light curves for these stars, with the downside that it cannot distinguish stars in crowded fields. It has been used to extract the light curves of 102 saturated stars observed by *Kepler* (Pope et al. 2019a). The other, more precise, method is halo photometry (White et al. 2017; Pope et al. 2019b). Halo photometry works by performing photometry in the halo of the point spread function (PSF), where weights are fitted to each pixel by minimizing an objective function. Halo photometry was inspired by the approach used by Aerts et al.

* E-mail: jrud0912@uni.sydney.edu.au

(2017) for the O9.5Iab star HD 188209 and has similarities to the Optimized-Weight Linear (OWL) photometry concept described by Hogg & Foreman-Mackey (2014). Halo photometry has successfully been used with *K2* for: the seven brightest stars in the Pleiades (White et al. 2017), α Tau (Aldebaran; Farr et al. 2018), ρ Leo (Aerts et al. 2018), ι Lib (Buyschaert et al. 2018), ϵ Tau (Arentoft et al. 2019), and 162 saturated stars observed in *K2* (Pope et al. 2019b). With TESS it has been used for α Aql (Altaïr; Rieutord et al. 2024), and the two brightest stars in the Scorpius-Centaurus Association, β Cen and α Cru (Sharma et al. 2022). However, halo photometry can be limited by both crowding, which dilutes the stellar signal in the halo pixel, and variations in the background, as shown for the third-magnitude star τ Ceti (Eisner et al. 2019), which caused a false transit to appear in the halo photometry light curve.

In this paper, we perform halo photometry on 98 of the brightest saturated stars observed by TESS in Sectors 1–93. These stars range from the brightest second-magnitude stars up to most of the zeroth-magnitude stars. They include almost all of the brightest red giants (RGs), where it is possible to determine v_{\max} for 13 of them, allowing us to estimate masses. The sample also includes some of the brightest known δ Scuti stars, γ Doradus stars, slowly pulsating B-type (SPB) stars, β Cephei variables, stochastic low-frequency variables (SLFs), eclipsing binaries (EBs), as well as other types of variable stars such as long-period variables (LPVs) and α^2 CVn variables. For some of these stars, this study reports the first detection of stellar variability.

Among the stars in our sample, we found three highlights. The first is the second magnitude A7IV-V star α Cep (Alderamin), which we discovered to be a δ Sct- γ Dor hybrid pulsator using 11 TESS sectors. Secondly, we found that the binary system ϵ Car (Avior) is either an asteroseismic binary consisting of an LPV and an SPB star, or an LPV star with an α^2 CVn companion. Lastly, there is the multiple system γ And (Almach), in which we discovered two of the components to be eclipsing.

We structure this paper as follows. In Section 2, we describe the selection process of our sample. In Section 3, we describe the extraction of our light curves using halo photometry and comparison with pipeline light curves. We will then present results for oscillating RGs (Section 4), pulsating A/F stars (Section 5), pulsating O/B stars (Section 6), and EBs (Section 7). In Section 8, we compare the halo photometry results from TESS with the *K2* Bright Star Survey (Pope et al. 2016) and compare the halo photometry amplitudes with previous measurements for EBs. In Section 9, we explore potential synergies with the PLANetary Transits and Oscillations of stars (PLATO; Rauer et al. 2025) and the Stellar Observations Network Group (SONG; Andersen et al. 2014; Grundahl et al. 2017; Kjeldsen et al. 2025).

2 THE TESS HALO SAMPLE

We selected our sample using the Hipparcos and Tycho catalogues (Perryman et al. 1997; Høg et al. 1997; van Leeuwen et al. 1997; ESA 1997), since the *Gaia* catalogue (Gaia Collaboration et al. 2023) is not complete for bright stars. We selected all stars with magnitudes brighter than 2.66 in V . We chose this cut to avoid overlap with the “TESS Luminaries Sample” of solar-like-oscillators by Lund et al. (2025), whose brightest star is the subgiant η Boo ($V = 2.68$). Since they successfully used a standard photometric method to extract the light curves for their stars, we did not see the need to include fainter stars.

We excluded the eight brightest stars ($V \leq 0.40$) because they require special treatment, due to the poor smear correction and a lack of

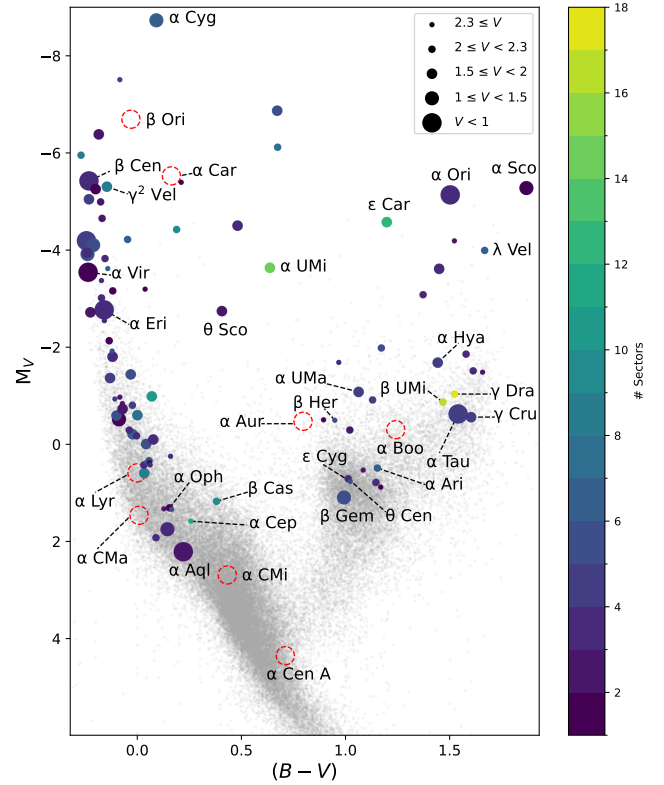


Figure 1. A CMD showing the stars in our sample in the Hipparcos and Tycho catalogues, coloured based on the number of TESS sectors available, overlaid on the background of the Hipparcos stars. The size of the dots corresponds to the V mag. The red circles are the brightest stars, which we excluded from our sample. Various prominent and interesting stars are highlighted in the figure.

halo pixels containing the stellar variability (Sirius, Canopus, α Cen, Arcturus, Vega, Capella, Rigel, and Procyon). We also excluded two stars, α Peg (Markab) and β Sco (Acrab), that were not observed by TESS as of Sector 93. Finally, we added the RG β Her (Kornephoros) to our sample, despite it having an apparent magnitude of $V = 2.78$, because it had a small target pixel file (TPF), which did not encompass the entire bleed. We include a sample of 98 stars in this paper, with data from a total of 411 TESS sectors.

Using both the Hipparcos parallaxes and apparent V -band magnitude, we calculated the absolute magnitude (M_V). We used the calculated M_V and the colour ($B - V$) to plot the stars in a colour-magnitude diagram (CMD) shown in Fig. 1, where we colour-code the stars by the number of TESS sectors available. The CMD shows that most of our stars are either O-B-A-F dwarfs or evolved stars such as RGs. We also see from Fig. 1 that the number of available TESS sectors ranges from 1 to 18; none of the stars in our sample are in the northern or southern TESS continuous viewing zone (CVZ). We list the stars in Table A1, providing their names, TIC, HD, V , $B - V$, M_V , spectral types, number of sectors (N), number of good HALOPHOT sectors (N_H , see Section 3.3), number of good pipeline sectors (N_P , see Section 3.3), and variability classification. We obtained the spectral types from the Yale Bright Star Catalog (5th ed.; Hoffleit & Warren 1995).

3 PROCESSING OF THE LIGHT CURVES

3.1 Halo photometry

Halo photometry measures flux variations in the unsaturated halo of the PSF by masking the saturated pixels. The remaining pixels are then assigned weights by minimising an objective function, whereafter a light curve is created by summing the weighted pixels (White et al. 2017; Pope et al. 2019b). Halo photometry has the advantage over standard aperture photometry by ignoring the saturated pixels and not needing larger aperture mask to encompass the bleed. We provide a brief summary of the method.

We can describe the halo flux in a given image as:

$$f_i = \sum_{j=1}^N w_j p_{ij}, \quad (1)$$

where i is the image index, N is the number of pixels, w_j is the weight of the pixel j , and p_{ij} is the flux of pixel j in the image i . All of the weights are defined to be non-negative and must sum to unity. The weights are assigned to the pixels by minimising an objective function, chosen to be Total Variation (TV) given by:

$$TV = \frac{\sum_{i=1}^M |f_i - f_{i-1}|}{\sum_{i=1}^M f_i}, \quad (2)$$

where M is the total number of observations. See Pope et al. (2019b) for more details.

For this work, we used an implementation of halo photometry closely following the PYTHON module HALOPHOT¹, with a modification in solving the objective function compared to Pope et al. (2019b). We used the PYTHON framework JAX² (Bradbury et al. 2018) to both calculate and solve the objective optimisation instead of AUTOGRAD and SCIPY, as was done by Pope et al. (2019b). The objective function itself was solved by using the L-BFGS algorithm implemented in the JAX module JAXOPT³ (Blondel et al. 2021). We also note that our pixel masking differs slightly from HALOPHOT, in that we also exclude the pixels immediately above and below the saturated pixels. We did this to avoid the pixels at the edge of the bleed columns, which would otherwise inflate the amplitude of the stellar variability. All of these changes have been implemented in the current version of HALOPHOT.

3.2 Extraction of the light curves

To obtain the TPFs of all of the stars in our sample, we used TESScut (Brasseur et al. 2019) with a pixelcut of 31×31 in the Full Frame Images (FFIs). We chose this dimension to obtain a sufficient number of halo pixels and include the background around the star, noting there is no need to encompass the entire bleed column.

To fit the background model, we used the PYTHON module TESSBKG⁴, which fits a spatially varying model using the background pixels. It has previously been used to fit the background of the third magnitude star ι Dra (Hill et al. 2021; Campante et al. 2023). Unlike those studies, we fitted the background with a linear model instead of a second-order polynomial, but we note that the choice of model had minimal effect on the extracted light curves. We then used the background fit from TESSBKG to remove all pixels for which the ratio between the fitted background and the median flux was greater than

0.3. We did this to remove most of the background stars, which could cause contamination. For the bright background stars, we masked them after inspecting the TPFs visually.

For the halo photometry, we ran HALOPHOT twice. The first fit was used to identify and remove outlier cadences and those with zero flux via sigma clipping. We also removed sections affected by earthshine and moonshine. These cadences have high flux in the beginning and end of each TESS orbit, and were removed by manually masking these cadences after visual inspecting the initial light curves. We did this to improve our HALOPHOT fit, since these epochs would dominate the light curve variability and influence the TV fit. A few of the TPFs contained single pixels with high weights, which we masked to prevent them from dominating the light curve. We then recalculated the pixel weights for the second and final HALOPHOT fit.

3.3 Quality of halo photometry

To evaluate the quality of the extracted HALOPHOT light curves, we downloaded the pipeline light curves from Mikulski Archive for Space Telescopes (MAST)⁵ using the PYTHON module LIGHTKURVE (Lightkurve Collaboration et al. 2018). We used the 120-s cadence light curves from TESS Science Processing Operations Center (SPOC; Jenkins et al. 2016), when they were available, and TESS-SPOC light curves from the FFIs (Caldwell et al. 2020) when they were not. If the TESS-SPOC light curve was also not available, we used light curves from the Quick-Look Pipeline (QLP; Huang et al. 2020a,b; Kunimoto et al. 2021, 2022). In the few cases where the QLP light curve was also unavailable (6 sectors), we created our own custom aperture photometry using LIGHTKURVE, using the same available pixels as in HALOPHOT but without TV minimisation.

We used the method described in Section 4 of Kjeldsen et al. (2025) to de-trend the time series using a high-pass filter and remove outliers. We tailored the high-pass filter width for each star to preserve the stellar signal in the light curves. Afterwards, we assigned variability classification to all of our stars by looking at their light curves and Fourier spectra from both HALOPHOT and pipeline. From the HALOPHOT, SPOC, QLP, and custom aperture light curves, we found that 77 out of 98 stars show variability.

We made two kinds of diagnostic plots for our targets: single-sector and all-sectors. We show examples of single-sector diagnostic plots in Fig. 2 for the δ Sct variable α Oph (Rasalhague) in Sector 79, and in Fig. 3 for the SLF variable ζ Pup (Naos) in Sector 61. In Fig. 4 we show an example of an all-sectors plot for the RG β Gem (Pollux) across all available TESS sectors. Each diagnostic plot shows the time series and Fourier spectrum from both the HALOPHOT and pipeline light curves. The all-sectors plots contain the spectral type, the V magnitude, our variability classification, and the width of the high-pass filter used for de-trending. The single-sector diagnostic plots contain the time series, the flux map, the HALOPHOT weightmap, and the power spectra, for the given sector. They also contain information about the quality of HALOPHOT and pipeline light curves. We compiled three sets of diagnostic plots: the first for classical pulsators and EBs, the second RGs and LPVs, and the third for SLFs. All the diagnostic plots are available on GitHub⁶.

To compare the HALOPHOT light curves with SPOC, TESS-SPOC, QLP, and with our custom non-TV-minimised light curves, we examined both the time series and the power spectrum to assess the quality.

¹ <https://github.com/hvidy/halophot>

² <https://github.com/google/jax>

³ <https://github.com/google/jaxopt>

⁴ <https://github.com/hvidy/tessbkgd>

⁵ <https://mast.stsci.edu/portal/Mashup/Clients/Mast/Portal.html>

⁶ https://github.com/JonatanRudrasingam/TESS_halophot

More specifically, we examined the scatter and systematics in the time series, the signals in the power spectrum and, for multi-sector stars, the quality of the light curve and Fourier spectrum relative to other sectors. For each sector, we rated the HALOPHOT and pipeline light curves as either good or poor. The number of good HALOPHOT light curves, N_H , and the number of good pipeline light curves, N_P , are listed in Table A1 for each star.

Our inspections of the results revealed several trends. Firstly, the QLP light curves for our sample are nearly always of lower quality than the HALOPHOT light curves. This can be explained by the circular aperture mask used by QLP, which is not well-suited to saturated stars. For stars without SPOC or TESS-SPOC light curves, the best available light curves are therefore from HALOPHOT. Secondly, the best SPOC light curves are comparable to the best HALOPHOT light curves, although about 79 SPOC light curves have poorer quality than the HALOPHOT counterpart, especially at the bright end of our sample. SPOC light curves can be degraded by either poor aperture masks or TPFs that fail to encompass the entire bleed column. For very bright stars, the saturated columns will not only be large, requiring larger TPFs and aperture, but they can also show non-linear effects, complicating the photometry. An exception is the brightest star in our sample, α Eri (Achernar), which has a single SPOC light curve, that is comparable to HALOPHOT. Meanwhile, 35 HALOPHOT light curves are worse than their SPOC counterparts, which can be explained by contamination from background stars. For example, this is the case for the recently discovered α^2 CVn variable β Tau (Begari et al. 2026), where multiple background stars contaminate the unsaturated halo pixels.

For some variable stars, the SPOC light curves have lower amplitudes than the HALOPHOT even when both light curves appear to have comparable quality. The low amplitudes occur because the SPOC aperture mask does not fully encapsulate the bleed columns, which dilutes the stellar variations. Examples of this can be seen in Fig. 2 for α Oph, and in Fig. 3 for ζ Pup, where the SPOC amplitudes are significantly lower. For stars that have comparable light curves, like ζ Pup in Sector 61, but different amplitudes, we rated the light curves equally. However, we recommend using HALOPHOT light curves, especially if the amplitude is important for the given study. Whether the amplitudes from HALOPHOT are reliable is discussed in Section 8.2.

For the β Cep star α Cru, we assigned poor quality to all the SPOC light curves, despite the light curves themselves being comparable to HALOPHOT. We made this choice because the SPOC amplitude spectrum has a peak at $\sim 0.81 \text{ d}^{-1}$, which we attribute to the star HD 108250 ($V = 4.8$), which is inside the bleed column of α Cru. Masking pixels close to the position of HD 108250 removed the signal from the HALOPHOT light curves. This is an interesting case in which contamination has a greater effect on aperture photometry than on halo photometry.

For most of our EBs, except for α Gem (Castor) and λ Sco, the HALOPHOT light curves are generally better than the pipeline light curves, with larger eclipse depths that are consistent with published values (see Section 8.2). For the RGs and LPVs, our HALOPHOT light curves are generally better than pipeline light curves because most of them only have QLP light curves. Another detail is that stars fainter than $V = 2.55$ mostly either have comparable or worse HALOPHOT light curves than SPOC, with a few exceptions. This result is consistent with the fact that the aperture photometry method works for stars $\geq 2.68 V$ (Lund et al. 2025). An exception is the RG β Her ($V = 2.78$), where all 5 SPOC light curves have poorer quality than the HALOPHOT light curves due to small TPFs (see Lund et al. 2025). So HALOPHOT light curves are almost always better than QLP light curves, and they are comparable to SPOC light curves, with

HALOPHOT being better for the brightest stars, and SPOC being better for the fainter stars. However, the amplitudes for SPOC are sometimes lower than HALOPHOT due to poor aperture masks.

4 RESULTS FOR OSCILLATING RED GIANTS

We identified 15 RGs in our sample based on their spectral type, position in the CMD, light curves, and power spectra. RGs are known to have stochastic oscillations excited and damped by the turbulence in the convective envelope, which is the same mechanism that drives oscillations in the Sun (Chaplin & Miglio 2013). These solar-like oscillators show characteristic features in their power spectra, which can be used to make inferences about their physical properties. The first is the large frequency separation, $\Delta\nu$, between modes with the same angular degree, while the second is the frequency at maximum power, ν_{\max} . Ulrich (1986) showed that $\Delta\nu$ scales approximately with the mean density of a star:

$$\Delta\nu \propto \sqrt{\bar{\rho}}. \quad (3)$$

Meanwhile, ν_{\max} scales approximately with the acoustic cut-off frequency of the atmosphere (ν_{ac}), which in turn is related to the surface gravity and the effective temperature (Brown et al. 1991; Kjeldsen & Bedding 1995; Belkacem et al. 2011):

$$\nu_{\max} \propto \nu_{\text{ac}} \propto g/\sqrt{T_{\text{eff}}}. \quad (4)$$

Rearranging these two equations yields scaling relations for both mass and radius (Stello et al. 2008; Kallinger et al. 2010). However, we were only able to determine $\Delta\nu$ for one star, β Gem (Pollux; see Section 4.2). The remaining RGs have low ν_{\max} and too few sectors to resolve $\Delta\nu$. If only ν_{\max} is available, we can instead use a different scaling relation assuming the radius is known:

$$\frac{M}{M_{\odot}} \approx \left(\frac{\nu_{\max}}{\nu_{\max,\odot}} \right) \left(\frac{R}{R_{\odot}} \right)^2 \left(\frac{T_{\text{eff}}}{T_{\text{eff},\odot}} \right)^{1/2}. \quad (5)$$

Due to their brightness, all our RGs have published angular diameters and parallaxes, so equation (5) can be used. Using this scaling relation, we aimed to determine the approximate masses of the RGs in our sample without relying on detailed stellar modelling.

We used published radii from interferometry, mostly obtained with the Navy Precision Optical Interferometer (NPOI; Armstrong et al. 1998). For three stars that did not have NPOI measurements, α Phe, ϵ Sco, and θ Cen, we only had so-called radiometric angular diameters from Cohen et al. (1999), which we used along with the Hipparcos parallax to derive their radii. For T_{eff} , we used the same interferometric sources (Baines et al. 2018, 2021, 2023, 2025), except for Aldebaran (Strassmeier et al. 2018), α Phe (Charbonnel et al. 2020), ϵ Sco (Paegert et al. 2022), and θ Cen (Ottoni et al. 2022). Note that some of the uncertainties are unrealistically small, but we kept with the published values since they make a negligible contribution to the error budget.

To derive ν_{\max} from the TESS light curves, we first calculated the weighted power spectrum density using the Lomb-Scargle method (Lomb 1976; Scargle 1982), with weights computed as described in Section 4 of Kjeldsen et al. (2025). We calculated the weights for each sector separately before combining the time series. To measure ν_{\max} we used the PYTHON module PYMON⁷ (Howell et al. 2025), which is a simplified version of the SYD pipeline (Huber et al. 2009; Chontos et al. 2022). We used an initial value of ν_{\max} determined

⁷ <https://github.com/maddyhowell/pyMON>

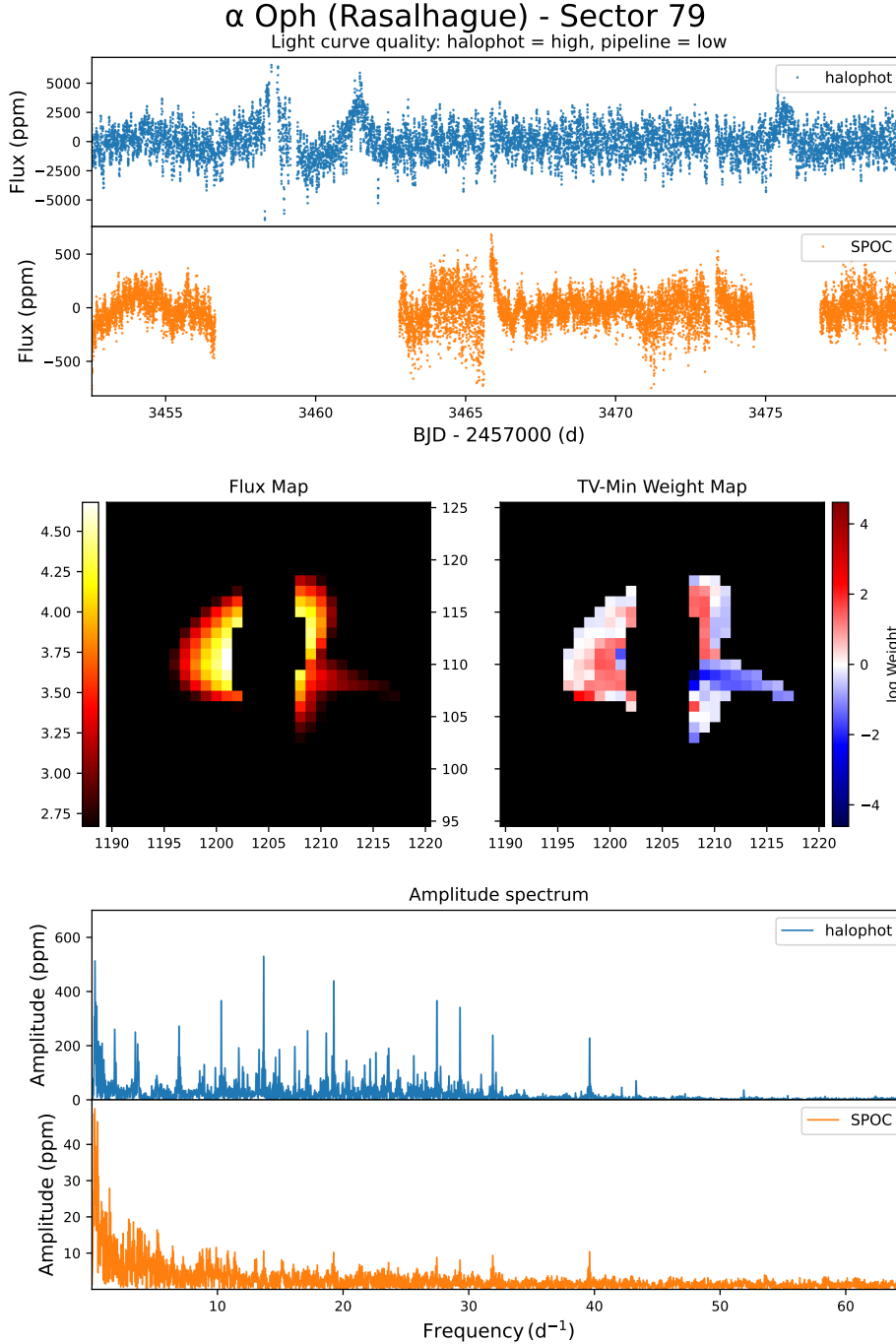


Figure 2. Single-sector diagnostic plots of the star α Oph (Rasalhague) in Sector 79. The top panel shows the HALOPHOT light curve in blue. The second panel shows the light curve from SPOC in orange. The middle two panels show the log-flux map (left) after masking of the saturated pixels and weightmap (right). The two bottom panels show the amplitude spectrum from both the HALOPHOT light curve and the SPOC light curve. The quality of the HALOPHOT and pipeline light curves are shown below the title.

by visual inspection of the power spectrum, and used a linear line in log-space as our background to derive ν_{\max} in PYMON.

To estimate approximate uncertainties for ν_{\max} , we used Fig. 5 from Hon et al. (2021), which shows the distribution of estimated fractional uncertainties for ν_{\max} from synthetic TESS data. Using this, we adopted uncertainties of 7 percent for ν_{\max} below $10 \mu\text{Hz}$, 6 percent for ν_{\max} between 10 and $20 \mu\text{Hz}$, 5 percent for ν_{\max} above $20 \mu\text{Hz}$, and 4 percent for β Gem (Pollux), with its ν_{\max} of $89.25 \mu\text{Hz}$.

We were able to determine ν_{\max} for 13 RGs. In Table 1 we list the RGs with measured ν_{\max} values, along with their T_{eff} , R , M , the angular diameter references, and the reference for the first asteroseismic detection. Among these RGs, five are newly detected solar-like oscillators. In Fig. 5, we show power spectra for 12 of them, along with their measured ν_{\max} values. Note that β Gem (Pollux), which has a high ν_{\max} than the rest, is discussed separately in Section 4.2.

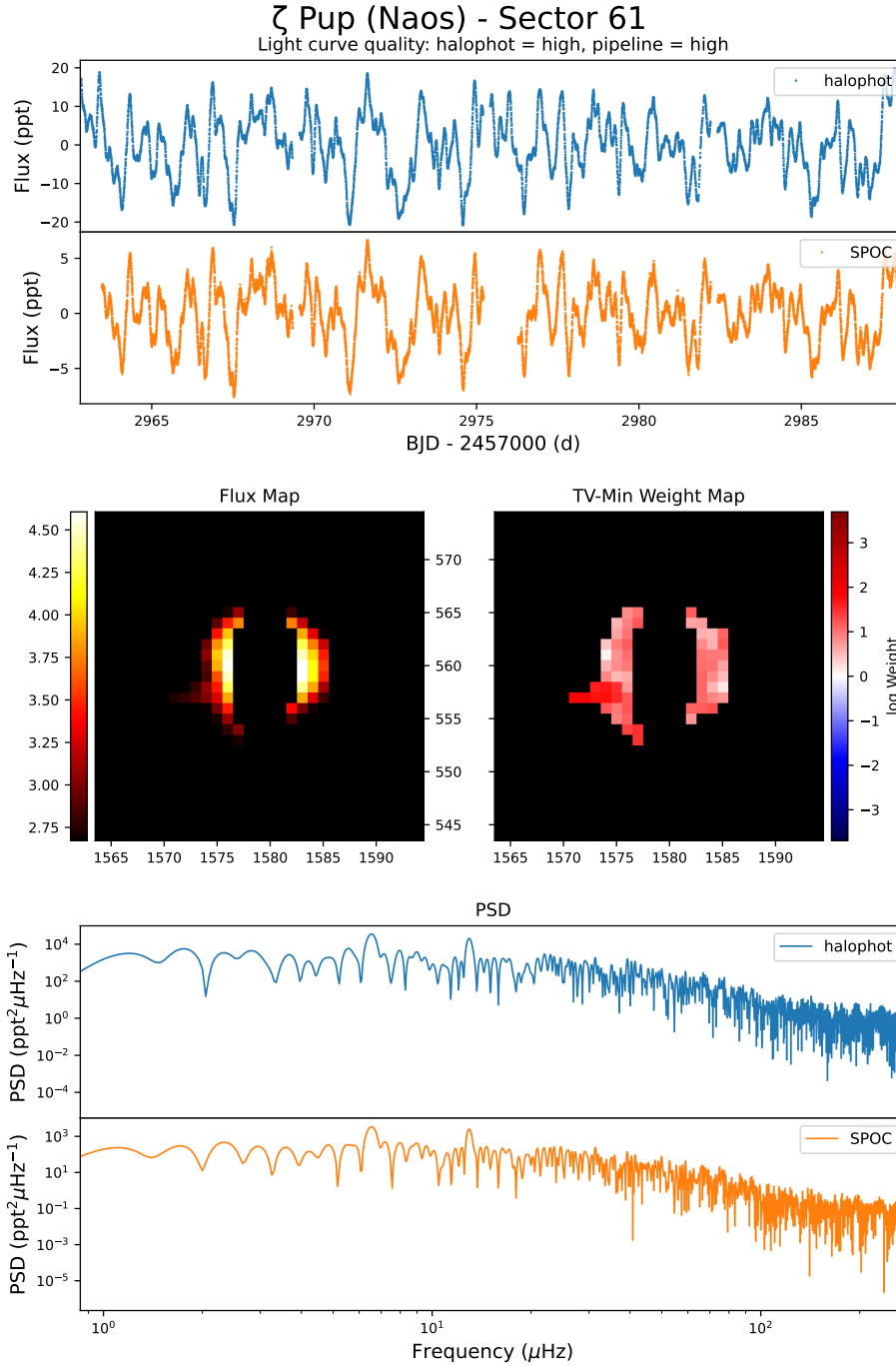


Figure 3. Similar single-sector diagnostic plots as Fig. 2, but for the SLF ζ Pup (Naos) in Sector 61. The only difference is that we plot the power spectral density on a log scale rather than the linear amplitude spectra in the bottom panels.

In Fig. 6 we show the asteroseismic HR-diagram for the RGs colour-coded by their radius.

For the remaining two RGs in our sample, γ Leo (Algieba) and α Ser (Unukalhai), we were not able to measure ν_{\max} , despite detecting variability.

4.1 α Tau (Aldebaran)

Aldebaran ($V = 0.87$) is the brightest RG in our sample. The presence of solar-like oscillations in Aldebaran was confirmed by Farr et al.

(2018) using RV variations from SONG-Tenerife, older archival observations, and halo photometry from K2. They derived a ν_{\max} value of $2.24^{+0.09}_{-0.08} \mu\text{Hz}$ and a mass of $1.16 \pm 0.07 M_{\odot}$. Our measured ν_{\max} ($1.99 \pm 0.10 \mu\text{Hz}$) and mass ($1.03 \pm 0.07 M_{\odot}$) are lower than their values, though our ν_{\max} is closer to their K2 value of $2.2 \pm 0.25 \mu\text{Hz}$. In Fig. 7 we show the power spectra from TESS and K2 for Aldebaran.

Earlier research suggested that Aldebaran hosted a planet with an orbital period of ~ 629 days (Hatzes & Cochran 1993, 1998b; Hatzes et al. 2015; Farr et al. 2018). However, recent studies have raised doubts over this claim. A study by Hatzes et al. (2018) of

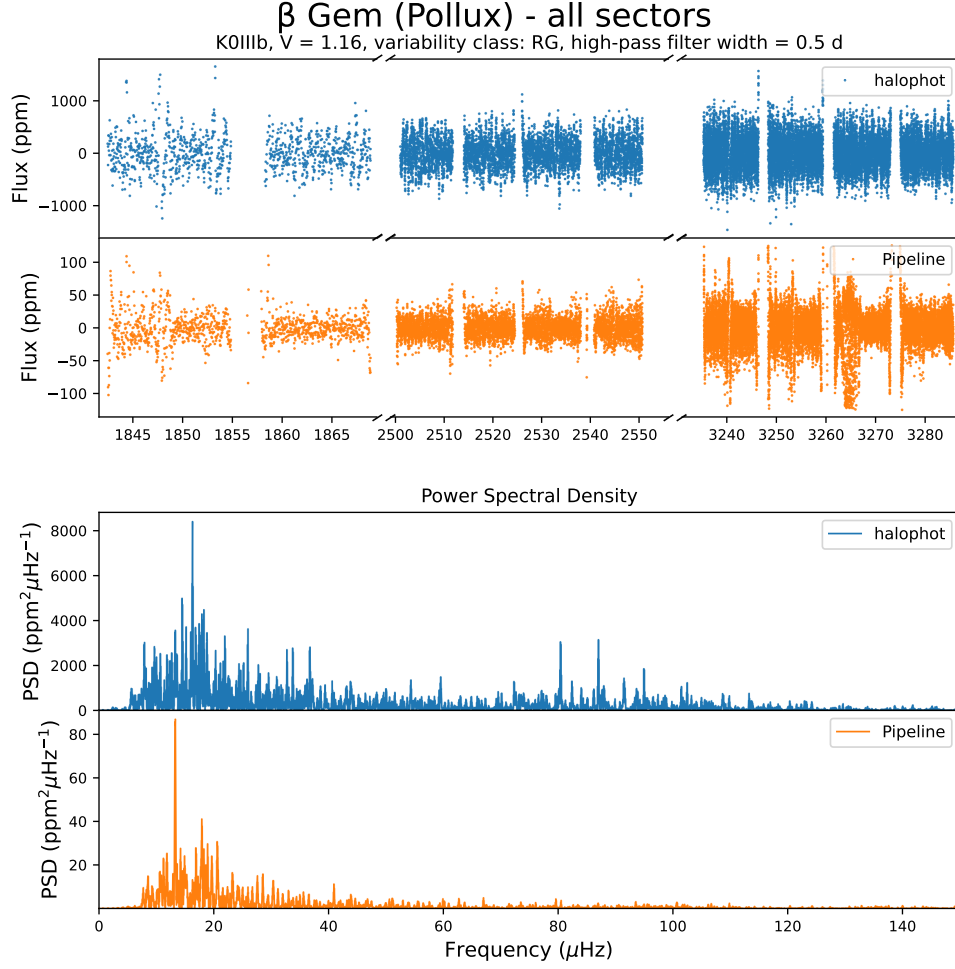


Figure 4. All-sector diagnostic plots of the RG β Gem (Pollux). The top panel shows the HALOPHOT light curve in blue. The second panel shows the light curve from the pipeline in orange. In this case the pipeline light curves are exclusively from QLP. The two bottom panels show the power spectral density from both the HALOPHOT light curve and the pipeline aperture light curve. The spectral type, V magnitude, variability class, and the width of the high-pass filter are shown below the title.

Table 1. List of 13 RGs with ν_{\max} determined from PYMON.

Star	ν_{\max} (μHz)	T_{eff} (K)	R (R_{\odot})	M (M_{\odot})	Angular diameter reference	First asteroseismic discovery
α Tau	1.99 ± 0.10	3900 ± 50^1	44.20 ± 0.90	1.03 ± 0.07	Farr et al. (2018)	Farr et al. (2018)
γ Dra	2.92 ± 0.15	3964 ± 29	51.80 ± 0.26	2.10 ± 0.11	Baines et al. (2021)	Hatzes & Cochran (1998a)
β UMi	3.16 ± 0.16	4008 ± 37	44.13 ± 0.22	1.66 ± 0.09	Baines et al. (2021)	Tarrant et al. (2008)
α Cas	9.68 ± 0.48	4625 ± 37	42.15 ± 1.55	4.98 ± 0.45	Baines et al. (2025)	This work
ϵ Boo	12.90 ± 0.65	4755 ± 66	37.61 ± 1.38	5.36 ± 0.48	Baines et al. (2021)	This work
α UMa	14.54 ± 0.73	4810 ± 22	27.33 ± 0.49	3.21 ± 0.20	Baines et al. (2025)	Buzasi et al. (2000)
α Phe	18.12 ± 0.91	4770 ± 250^2	13.39 ± 0.29	0.96 ± 0.07	Cohen et al. (1999)	This work
α Ari	22.06 ± 1.10	4373 ± 12	15.19 ± 0.10	1.43 ± 0.08	Baines et al. (2023)	Kim et al. (2006)
ϵ Sco	29.60 ± 1.50	4489 ± 40^3	12.91 ± 0.25	1.41 ± 0.09	Cohen et al. (1999)	Kallinger et al. (2019)
ϵ Cyg	34.94 ± 1.75	4659 ± 6	12.41 ± 0.29	1.56 ± 0.11	Baines et al. (2023)	Kallinger et al. (2019)
θ Cen	36.95 ± 1.85	4853 ± 41^4	10.96 ± 0.20	1.32 ± 0.08	Cohen et al. (1999)	This work
β Her	36.98 ± 1.85	5092 ± 64	15.92 ± 0.41	2.85 ± 0.21	Baines et al. (2018)	This work
β Gem	89.25 ± 3.57	4796.0 ± 10	8.92 ± 0.37	2.09 ± 0.26	Baines et al. (2025)	Hatzes & Zechmeister (2007)

1: Strassmeier et al. (2018), 2: Charbonnel et al. (2020), 3: Paegert et al. (2022), 4: Ottoni et al. (2022)

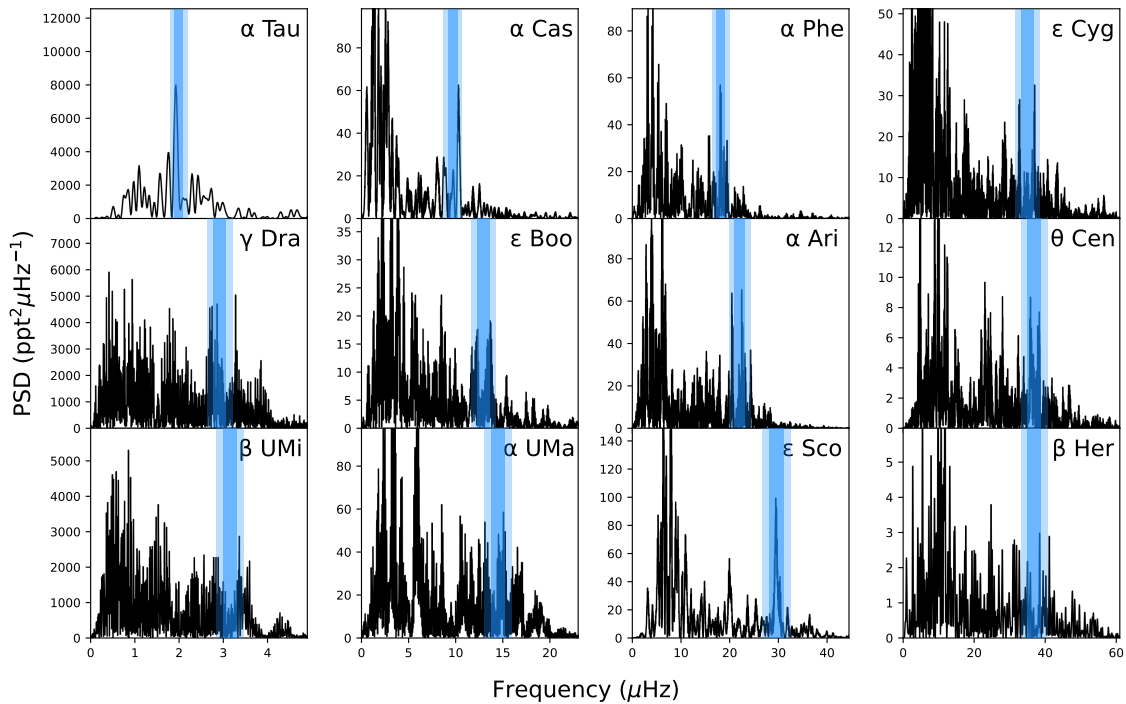


Figure 5. Power spectral density for 12 RGs with measurable ν_{\max} . The first column shows the PSD in the range 0–5 μHz , the second in the region 0–23 μHz , the third at 0–44.5 μHz , and the fourth at 0–61 μHz . The blue shaded regions indicate 1σ and 2σ uncertainties of the derived ν_{\max} . We note that β Gem (Pollux) is not included in this figure.

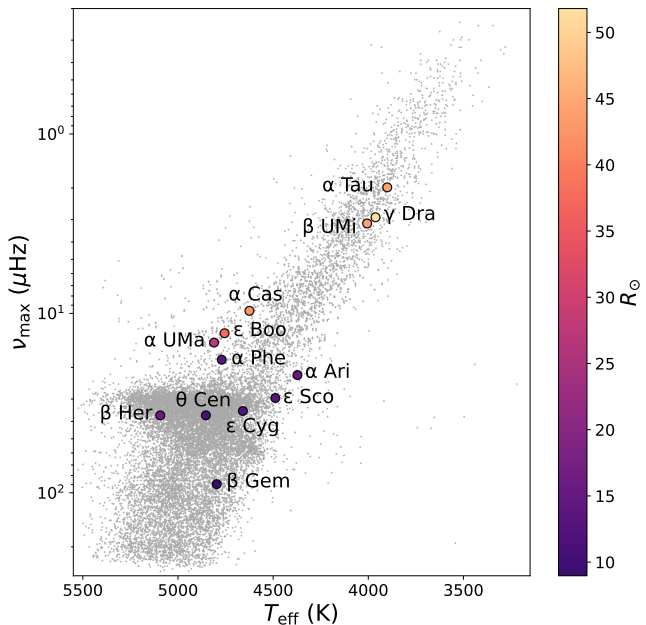


Figure 6. An asteroseismic HR diagram showing the ν_{\max} and T_{eff} of RGs in our sample colour-coded by their radius. Shown in grey are the RGs from Yu et al. (2018) and the LPVs from Yu et al. (2020).

γ Dra, which has a long-term RV signal similar to that of Aldebaran, showed that its RV signal disappeared and reappeared with a phase shift. This behaviour would be inconsistent with an RV signal of planetary origin. Later, Reichert et al. (2019) reanalysed the RV data

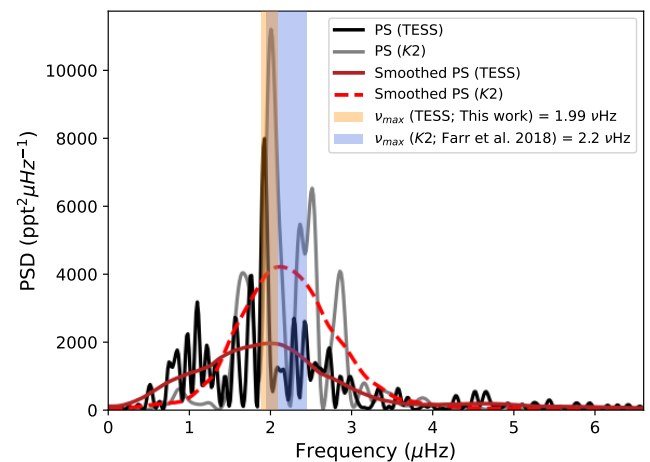


Figure 7. The power density spectrum of α Tau (Aldebaran) from both TESS (black) and *K2* (gray). The smoothed spectra, which were smoothed with an Epanechnikov filter (Epanechnikov 1969), with a width of 2 μHz , are shown as a dark red solid line (TESS) and as a red dashed line (*K2*). The orange shaded region represents 1σ region of the derived ν_{\max} from pYMON, while the blue shaded region represents 1σ region of the *K2* ν_{\max} from Farr et al. (2018).

of Aldebaran with additional results from Lick Observatory, and they concluded that while a two-planet system fits the results better than one planet, it would be dynamically unstable.

Aldebaran was observed by SONG, BRITe-Lem, and BRITe-Toronto to measure the amplitude ratio and phase shift between the asteroseismic signal in RV and in photometry (Beck et al. 2020),

which coupled with the newly available TESS data could yield a more detailed asteroseismic analysis of Aldebaran.

4.2 β Gem (Pollux)

Pollux ($V = 1.16$) is a K0IIIb giant and is one of the brightest RGs in our sample. Oscillations were discovered by [Hatzes & Zechmeister \(2007\)](#) using 20 h of RV observations, and further confirmed by [Hatzes et al. \(2012\)](#) using longer RV time series and photometry from MOST. Like Aldebaran, Pollux was also thought to have an exoplanet companion ([Hatzes & Cochran 1993](#); [Hatzes et al. 2006](#); [Reffert et al. 2006](#)). However, Pollux was shown to be weakly magnetically active ([Aurière et al. 2009, 2015](#)), with a periodicity similar to the claimed orbital period ([Aurière et al. 2021](#)), which might be the source of the RV signal.

Due to the high ν_{\max} , we were able to determine $\Delta\nu$ using échelle diagrams by aligning the $\ell = 0$ modes to be vertical, and with a value consistent with the empirical $\Delta\nu$ - ν_{\max} relation by [Yu et al. \(2018\)](#). To validate our $\Delta\nu$, we also calculated the autocorrelation function (ACF) and confirmed a peak near the found value. Using both the échelle method and the ACF, we found $\Delta\nu$ for Pollux to be $7.32 \pm 0.02 \mu\text{Hz}$. In [Fig. 8](#) we show the échelle diagram of Pollux, in which we can see the $\ell = 0, 2$ ridges located to the right, while the $\ell = 1$ modes are located to the left.

Using both ν_{\max} and $\Delta\nu$, we calculated the masses and radii for this star using the standard scaling relations. For the correction factor on $\Delta\nu$, $f_{\Delta\nu}$ ([Sharma et al. 2016](#)), we used Equation 16 by [Li et al. \(2023\)](#), with $[\text{Fe}/\text{H}] = 0.19$ from [Allende Prieto et al. \(2004\)](#). Using this equation yielded a seismic mass of $1.89 \pm 0.24 M_{\odot}$ and a seismic radius of $8.47 \pm 0.36 R_{\odot}$. The seismic radius is inconsistent with the interferometric radius of $8.97 \pm 0.03 R_{\odot}$ ([Baines et al. 2025](#)). When we used no correction, we obtained a mass of $2.12 \pm 0.26 M_{\odot}$ and radius of $8.97 \pm 0.37 R_{\odot}$, which is more consistent with the interferometric radius. Using [equation \(5\)](#) we obtained a seismic mass of $2.12 \pm 0.09 M_{\odot}$, which is consistent with the mass derived by not using $f_{\Delta\nu}$. If we used a different $f_{\Delta\nu}$ correction for red clump stars by [Schimak et al. \(2026\)](#), we obtained a seismic mass of $2.09 \pm 0.26 M_{\odot}$ and a seismic radius of $8.92 \pm 0.37 R_{\odot}$, which are consistent with the interferometric radius and the mass from [equation \(5\)](#). We list this radius and the corresponding mass for Pollux in [Table 1](#). While using this $f_{\Delta\nu}$ could suggest that Pollux is a red clump star, the position of Pollux in [Fig. 6](#) is also consistent with it ascending the red-giant branch.

Pollux has been extensively observed by SONG (see [Table B1](#) in [Appendix B](#)) and is currently monitored to better constrain the origin of its long-term RV variability. These observations can be used with the available TESS data to analyse the star asteroseismically, with detailed modelling of its well-defined modes.

4.3 α UMa (Dubhe)

α UMa ($V = 1.81$) is a binary system consisting of a K0III primary component ([Guenther et al. 2000](#)) and a A5V secondary component ([Gray 2018](#)). Solar-like oscillations were detected in the primary component by [Buzasi et al. \(2000\)](#), who used the 52-mm star camera on WIRE ([Buzasi 2000](#)), making it one of the first detections of solar-like oscillations using space-based photometry. They claimed the detection of 10 modes, ranging from 1.82 to 43.56 μHz , with a mode spacing of 2.94 μHz . The oscillation we detected in the power spectrum, along with the derived ν_{\max} of $14.54 \pm 0.19 \mu\text{Hz}$ confirmed the earlier detection from WIRE. However, we do not

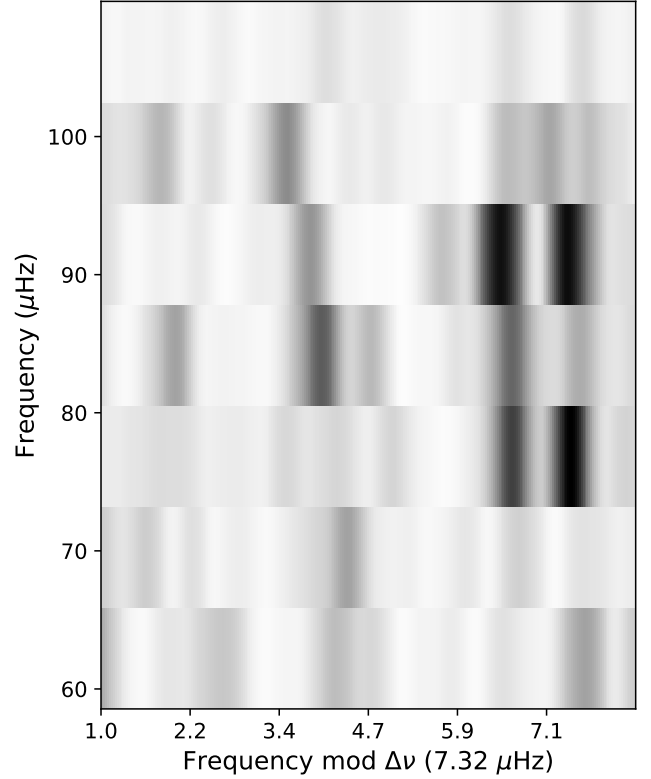


Figure 8. An échelle diagram of β Gem (Pollux) for $\Delta\nu = 7.32 \mu\text{Hz}$. The échelle is shifted by an offset of 1 μHz , since the $\ell = 0$ modes would otherwise be close to the right edge of the diagram.

detect modes below 9 μHz or above 18 μHz . A more in-depth study of the new HALOPHOT data and complementary SONG observations (see [Table B1](#) in [Appendix B](#)) could validate or refute the modes reported by [Buzasi et al. \(2000\)](#) and improve asteroseismic constraints for this star.

4.4 β UMi (Kochab)

β UMi ($V = 2.07$) is a bright RG and, with 16 TESS sectors, has the second-most sectors in our sample. Oscillations in the star were detected by [Tarrant et al. \(2008\)](#) using SMEI. They used ~ 1000 days of observation and were able to detect two modes at 2.44 and 2.92 μHz , which are consistent with our power spectrum. We also detected an additional mode around 3.37 μHz , which explains why we obtained a ν_{\max} above 3 μHz . We note that β UMi will be within 5° of the proposed northern PLATO field (see [Table 3](#)).

4.5 γ Dra (Eltanin)

This bright ($V = 2.24$) low- ν_{\max} RG, with 18 TESS sectors, has the most sectors in our whole sample. We detected oscillations in this star with ν_{\max} of $2.92 \pm 0.12 \mu\text{Hz}$. As mentioned in [Section 4.1](#), γ Dra has a similar long-term RV variation as Aldebaran ([Hatzes & Cochran 1993](#); [Hatzes et al. 2018](#)), which is unlikely to be of planetary origin ([Hatzes et al. 2018](#); [Ramirez Delgado & Dodson-Robinson 2020](#)). The star is inside PLATO's proposed northern field, within the field of view of its fast cameras (see [Table 3](#)).

4.6 α Cas (Schedar)

In α Cas ($V = 2.24$) we detected power excess at $10 \mu\text{Hz}$ in the star's power spectrum, which is the first reported detection of solar-like oscillations in the star. We report $\nu_{\text{max}} = 9.68 \mu\text{Hz}$ using pYMON and the derived mass using the scaling relation is $4.98 \pm 0.40 M_{\odot}$, which is unusually large for RGs (Crawford et al. 2024, 2025). The only other study which derived the mass of α Cas was by Reffert et al. (2015), who used stellar tracks from Girardi et al. (2000) to derive a mass of either 4.06 ± 0.35 or $3.98 \pm 0.30 M_{\odot}$. These values are lower than our derived mass, but are still relatively high for RGs. A further study of α Cas is needed in order to confirm the mass of the star.

4.7 β Her (Kornephoros)

The faintest star in our sample, β Her ($V = 2.78$), is a G7IIIa star, which we included because we noticed that the TPF did not encompass its bleed columns entirely. The star is a SB1 system (Campbell 1900; Plummer 1908; Eaton & Williamson 2007; Massarotti et al. 2008; Gray 2016), and its orbit was astrometrically resolved by Jancart et al. (2005) using Hipparcos data. If the projected semi-major axis and parallax are known, which is the case for β Her, then it becomes possible to determine the mass sum and mass ratio of an astrometric SB1 binary system (e.g. Videla et al. 2022). The star has been observed by CHARA/PAVO, enabling the determination of its angular diameter (Chowhan et al., in prep.) and is currently being monitored with SONG to constrain its orbit. Therefore, with asteroseismic independent mass and radius, β Her promises to be an asteroseismic benchmark star in the near future.

5 RESULTS FOR PULSATING A/F STARS

A-type and early F-type stars have a very thin surface convective layer, so the pulsations from these stars have a different origin than solar-like oscillators. In the classical instability strip we find the δ Sct variables, whose oscillations are driven by the κ -mechanism in the HeII ionisation zone (Goupil et al. 2005; Handler 2009) and turbulent pressure (Antoci et al. 2014, 2019).

In our sample, we detected five δ Sct variables by examining their amplitude spectra, their spectral type, and previous literature. These are α Aql (Altair), α Oph (Rasalhague), β Cas (Caph), α Cep (Alderamin), and δ Cas (Ruchbah). Their amplitude spectra are shown in Fig. 9, along with their expected fundamental modes, which we calculated using the luminosity-period relation from Barac et al. (2022). Among these five stars, we note that α Cep and δ Cas are newly discovered δ Sct variables.

Overlapping with the red edge of the classical instability strip and extending to redder colours in the HR diagram are the γ Dor variables, which are g-mode oscillators whose oscillations are excited by flux blocking at the base of their thin outer convection zone (e.g. Guzik et al. 2000; Dupret et al. 2005). We detected only one clear γ Dor variable, β Ari ($V = 2.64$), which was previously suspected to be a δ Sct variable (Barbiano di Belgioioso et al. 1983). However, both α Oph and α Cep show signs of multiple low-frequency peaks as discussed in Section 5.2 and Section 5.4.

Seven stars in our sample are chemically peculiar Ap and Bp stars. A small fraction of this class are rapidly oscillating Ap stars (roAp), which exhibit rapid variability (Kurtz 1990; Holdsworth et al. 2021). However, we did not detect any roAp signals in the 120-s cadence SPOC light curves among our Ap and Bp stars: α Eri

(Achernar), β Tau (Elnath; Begari et al. 2026), ϵ UMa (Alioth), α And (Alpheratz), ζ UMa (Mizar), γ Crv (Gienah), and θ Aur (Mahasim). For ϵ UMa, this confirms the earlier non-detection of oscillations by Retter et al. (2004), who used observation from the 52-mm star camera on WIRE.

5.1 α Aql (Altair)

Altair ($V = 0.76$) is the brightest known δ Sct variable, as discovered by Buzasi et al. (2005) using the 52-mm star camera on WIRE. Altair was then analysed by Le Dizès et al. (2021) using the observations from MOST, and by Rieutord et al. (2024) using halo photometry on TESS Sector 54.

5.2 α Oph (Rasalhague)

The binary system, α Oph ($V = 2.08$), consists of a primary rapidly rotating A5IV star and a K5V-K7V star as its companion (Hinkley et al. 2011). A previous asteroseismic study of this system was done by Monnier et al. (2010) using 30 days of observation from MOST. They confirmed that the primary star is a δ Sct + γ Dor hybrid. Our HALOPHOT amplitude spectrum (see Fig. 2) show clear detection of multiple peaks in the expected p- and g-mode frequency range, confirming the earlier detection.

We attempted to find $\Delta\nu$ for this star using the échelle diagram by aligning the $\ell = 1$ modes to be vertical (Bedding et al. 2020), since we know the dynamical mass and interferometric radius of the oscillating component. We found three possible values of $\Delta\nu$: 3.35, 3.37, and 3.50 d^{-1} . We chose 3.50 d^{-1} as the most plausible value and present its corresponding échelle diagram in Fig. 10. We compared this value to the theoretical $\Delta\nu$ calculated from the star's density, using the dynamical mass ($2.20 M_{\odot}$) from Gardner et al. (2021) and the interferometric radius ($2.623 R_{\odot}$)⁸ from Monnier et al. (2010). We obtained a theoretical $\Delta\nu$ of 3.44 d^{-1} , which matches the three possible $\Delta\nu$ values we found.

5.3 β Cas (Caph)

β Cas ($V = 2.28$) was discovered to be variable by Millis (1966), making it the third brightest δ Sct variable in our sample. Unlike the other δ Sct variables in our sample, β Cas has relatively few peaks in its amplitude spectrum. Zwintz et al. (2020) analysed β Cas using observations from BRITe, SMEI and TESS, along with spectropolarimetry observations, and found evidence that the star has a dynamo magnetic field.

5.4 α Cep (Alderamin)

A bright ($V = 2.45$) A7IV-V star (van Belle et al. 2006), α Cep was suspected to be a δ Sct variable by Hauck (1971). It was therefore listed as a possible variable in the General Catalogue of Variable Stars (GCVS⁹; Samus' et al. 2017), and as a δ Sct variable in The International Variable Star Index (VSX¹⁰; Watson et al. 2016), but apparently without observations of variability. The star was observed by BRITe (Zwintz et al. 2024), but they did not detect any variability. However, all 11 TESS sectors of this star show small-amplitude peaks

⁸ Calculated as the average between the equatorial ($2.858 R_{\odot}$) and polar radius ($2.388 R_{\odot}$)

⁹ <http://www.sai.msu.su/gcvs/gcvs/>

¹⁰ <https://www.aavso.org/vsx/index.php>

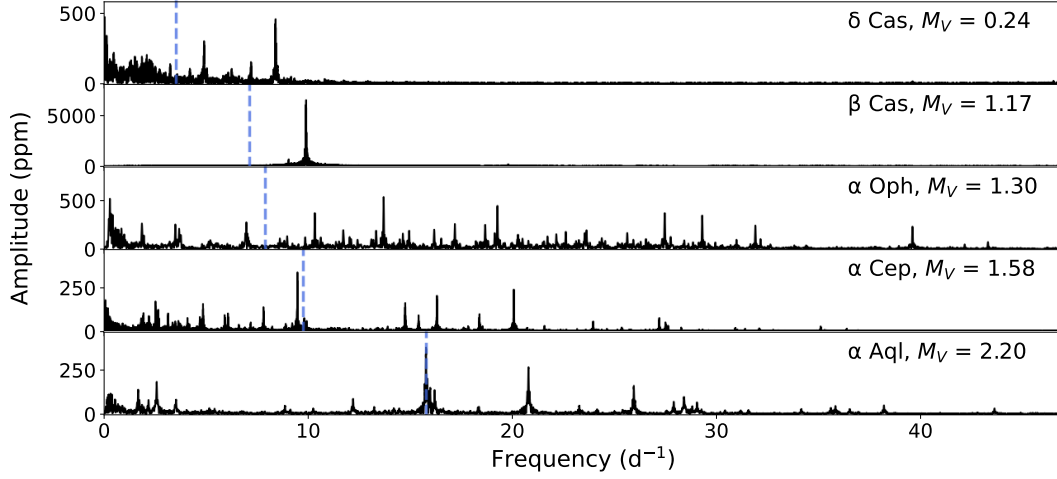


Figure 9. A gallery plot of the five δ Sct variables in our sample sorted by their M_V . The expected fundamental radial modes, calculated using luminosity-period relation from Barac et al. (2022), are shown as blue dashed lines.

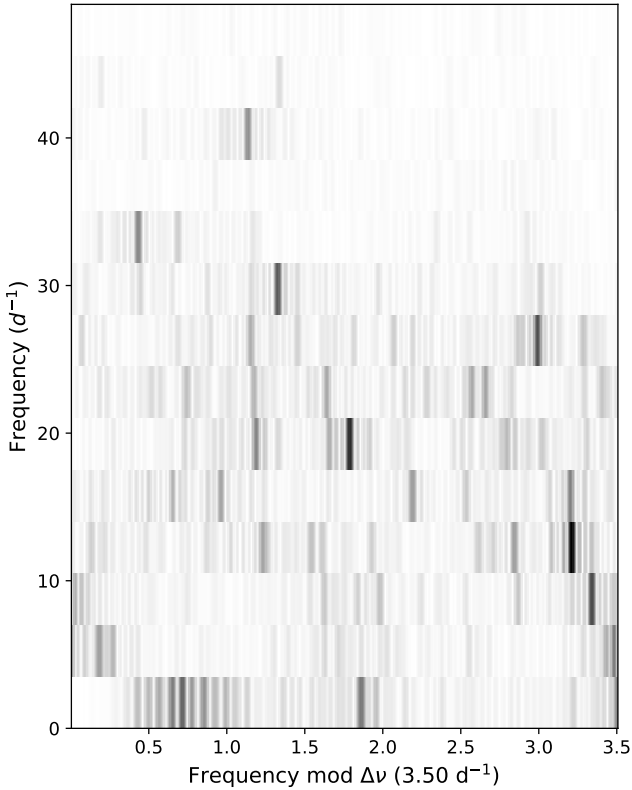


Figure 10. An échelle diagram of α Oph (Rasalhague) with the most plausible value of $\Delta\nu$.

characteristic of a δ Sct star, making it the brightest δ Sct variable discovered by TESS.

We also see multiple peaks below the expected frequency of the fundamental radial mode (~ 9.7 d^{-1} ; see Fig. 9). This value suggests classification of the star as a δ Sct + γ Dor hybrid. Furthermore, the star will be inside PLATO’s proposed northern field (see Table 3), and therefore has the potential to be one of the best-studied bright δ Sct- γ Dor hybrids in the future.

5.5 δ Cas (Ruchbah)

A newly discovered δ Sct variable, δ Cas ($V = 2.66$), is the second faintest star in our total sample. It was initially classified as an EB, with a period of 759 d, in the GCVS and was subsequently classified as such in Catalogue of Eclipsing Variables (Malkov et al. 2006; Avvakumova et al. 2013) and VSX (Watson et al. 2016). However, we did not see any eclipses in either the HALOPHOT or SPOC light curves. It was observed by BRITE (Zwintz et al. 2024), but they did not detect any variability. This does not rule out the possibility that the star is eclipsing due to the claimed orbital period; however, we note that the current GCVS lists the star as a non-variable (Samus’ et al. 2017).

6 RESULTS FOR PULSATING O/B STARS

Some O and B stars pulsate as β Cep variables, where the κ -mechanism drives the p- and g-mode oscillations in the iron opacity bump at $\sim 200,000$ K (Dziembowski & Pamiatnykh 1993; Thoul 2009). Of the stars in our sample, nine are β Cep variables, including the ellipsoidal (ELL) variable α Vir (Spica; Tkachenko et al. 2016) and the EB λ Sco (Shaula).

Cooler B-type stars can also be SPB stars, which are g-mode pulsators (Dziembowski et al. 1993). We detected three SPB stars and one candidate, ϵ Car, which might be an LPV + SPB asteroseismic binary (see Section 6.3). Additionally, Be-type stars have previously been found to exhibit photometric variability (e.g. Gutiérrez-Soto et al. 2007; Labadie-Bartz et al. 2017, 2022; Rivinius & Klement 2026). These are non-supergiant B-type stars that have or at some point had Balmer lines in emission (Collins 1987; Rivinius et al. 2013), which has been attributed to the presence of a circumstellar disk (e.g. Struve 1931; Carciofi et al. 2009). We classified eight stars in our sample as variable Be stars, including the brightest star, α Eri (Achernar).

Another form of variability observed in O and B stars is stochastic low-frequency (SLF) variability. These SLF variables are characterised in the frequency domain by a stochastic signal at low frequencies that decreases in power towards higher frequencies. The SLF variability was initially characterised for three O-type stars by Blomme et al. (2011) and was later found to be ubiquitous in massive

stars, including main-sequence O- and B-type stars (e.g. [Bowman et al. 2019a,b, 2020](#); [Pedersen & Bildsten 2025](#)), blue supergiants (e.g. [Bowman et al. 2019a, 2020](#); [Kourniotis et al. 2025](#)), yellow and red supergiants ([Dorn-Wallenstein et al. 2019](#); [Zhang et al. 2024](#)), and Wolf-Rayet stars (e.g. [Lenoir-Craig et al. 2022](#)). In our sample, we classified eight stars as SLFs and one star, θ Sco, as a potential SLF candidate (see [Section 6.2](#)). We show their weighted power spectral densities in [Fig. 11](#).

6.1 γ^2 Vel

γ^2 Vel ($V = 1.75$) is a SB2 system consisting of a WC8 Wolf-Rayet star and an O9I supergiant ([Hoffleit & Warren 1995](#)), with an orbital period of 78.53 d ([Schmutz et al. 1997](#)). Variability was detected by [Richardson et al. \(2017\)](#) using BRITe observations and 488 high-resolution optical spectra, and was attributed to colliding winds. We detected variability characteristic of SLF, potentially making it the brightest known Wolf-Rayet star with stochastic variability. The variability detected by [Richardson et al. \(2017\)](#) had a longer timescale than the SLF signal we observed. However, the BRITe amplitude spectrum ([Fig. 5](#) in [Richardson et al. 2017](#)) appears to show characteristics similar to the TESS SLF signal. We also detected a peak at 18.94 μHz , measured using sine-wave fitting ([Roberts et al. 1987](#)), which we show in [Fig. 12](#).

We note that γ^1 Vel ($V = 4.21$) is only 41" from γ^2 Vel ([Hernandez & Sahade 1980](#)), and could thus contaminate the light curves. A future study incorporating the TESS, BRITe, and PLATO (see [Table 3](#)) observations would help characterise the stochastic nature of this system even further. However, the question of saturation for γ^1 Vel and γ^2 Vel in PLATO could complicate the photometry.

6.2 θ Sco (Sargas)

θ Sco ($V = 1.86$) is binary system consisting of either a F1III ([Hoffleit & Warren 1995](#)) or a F1III ([Gray & Garrison 1989](#)) primary component, along with a $\sim A3$ giant secondary component ([Lewis et al. 2022](#)). The primary component is a rapid rotator, and could therefore be a post-merger object ([Lewis et al. 2022](#)). BRITe flagged the star as a variable ([Zwintz et al. 2024](#)) and we detected SLF-like variability in both TESS sectors.

6.3 ϵ Car (Avior)

A long-period binary system consisting of a K3III primary component and a B2:V secondary component ([Hoffleit & Warren 1995](#)), which are 0.41" apart ([Parsons & Ake 1998](#)), ϵ Car ($V = 1.86$) was flagged by BRITe as a variable ([Zwintz et al. 2024](#)) and the secondary component was previously analysed by [Bowman et al. \(2022\)](#) using TESS, but they ruled out β Cep pulsations in the star. From the HALOPHOT light curves, all 12 TESS sectors revealed a frequency signal at 13 μHz and a low frequency background signal, which we show in [Fig. 12](#). The frequencies, along with their spectral types, could point to ϵ Car being an LPV + SPB asteroseismic binary. Alternatively, the companion was classified as a B2Vp star by [Parsons & Ake \(1998\)](#), suggesting that it could be an α^2 CVn variable. Finally, we note that this system is within PLATO's southern field (see [Table 3](#)), potentially providing a long time series for detailed asteroseismology.

6.4 σ Sgr (Nunki)

σ Sgr ($V = 2.05$) is an interferometric binary ([Hanbury Brown et al. 1974](#); [Bedding et al. 1994](#)). The star was analysed by [Telting et al. \(2006\)](#) using ground-based spectrographs and later by [Bowman et al. \(2022\)](#) using TESS for β Cep pulsations, but neither studies detected any sign of variability. The light curve for this star showed some variability and multiple peaks in the amplitude spectrum below 3 d^{-1} , although with only one sector, the peaks are not resolved enough. We classified the star as a SPB variable.

7 RESULTS FOR ECLIPSING BINARIES

If the orientation of two binary components aligns such that one or both produce periodic dips in the light curve, then the system is classified as an EB. The depth and shape of the eclipses depend on the relative size of the components, their temperatures, and the orientation of their orbit. EBs observations can be complemented by RV observations to determine model-independent masses and radii for both components. The derived masses and radii can be used to test stellar models (e.g. [Higl & Weiss 2017](#)) and, in a few cases, combined with asteroseismic results (e.g. [Gaulme et al. 2016](#); [Li et al. 2018](#); [Benbakoura et al. 2021](#); [Brogaard et al. 2022](#); [Gaulme et al. 2022](#); [Thomsen et al. 2025](#); [Southworth & Bowman 2025](#)).

Of the stars in our sample, 8 are EBs. Except for γ And, all were already known to be eclipsing, with λ Sco being the most recent discovered EB ([Buzasi et al. 2004](#); [Bruntt & Buzasi 2006](#)). In [Table 2](#) we list the EBs in our sample, along with the eclipsing components, the periodicity in days, and individual notes for some of them.

7.1 β Per (Algol)

Algol ($V = 2.09$) is one of the first known variable stars ([Montanari 1671](#)). [Goodricke \(1783\)](#) proposed that the variability could be caused by an object eclipsing the star, and the binary nature of the system was confirmed by [Vogel \(1890\)](#), who resolved the star as a spectroscopic binary.

There have been many photometric observations of Algol (e.g. [Stebbins 1910](#); [Chen & Reuning 1966](#); [Smyth et al. 1975](#); [Eaton 1975](#); [Longmore & Jameson 1975](#); [Zeilik et al. 1980](#); [Al-Naimiy et al. 1985](#); [Kim 1989](#)), and so the eclipse depth of this star is well known across a broad wavelength range. We therefore use Algol to validate the amplitude of the HALOPHOT light curves in [Section 8.2](#).

7.2 γ And (Almach)

γ And ($V = 2.10$) is a multiple system consisting of five stars. The brightest star, γ^1 And, is a K2+IIb giant ([Keenan & McNeil 1989](#)), which is 9.9" separated from its companion γ^2 And, which itself is an interferometric system consisting of γ And B and C. The B component was discovered to be an SB2 by [Maestre & Wright \(1960\)](#), who derived an orbital period of 2.670 days and an eccentricity of 0.292. The HALOPHOT light curves reveal an eclipsing binary with an orbital period of ~ 2.6 days, with secondary eclipses that are offset from the midpoints of the primary eclipses, showing that the system is eccentric. These properties of the eclipsing binary are consistent with the orbital parameters reported by [Maestre & Wright \(1960\)](#). We conclude that the B component is a newly discovered EB. Furthermore, the orbits of the B and C were resolved using speckle interferometry ([Docobo & Ling 2007](#)), making it one of the few

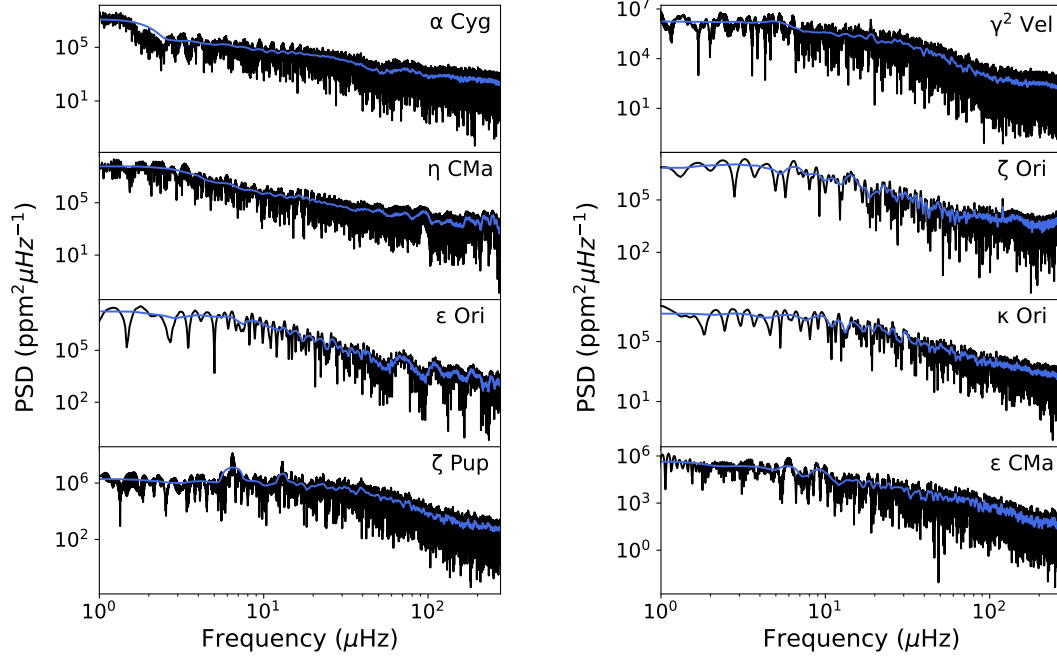


Figure 11. A gallery plot of the 8 SLFs in our sample. The weighted power spectral densities are shown in black. The smoothed spectra with an Epanechnikov filter (Epanechnikov 1969), with a width of $2 \mu\text{Hz}$, are shown in blue.

Table 2. List of EBs in our sample.

Star	V	Eclipsing components	Orbital period (d)	Period reference	Notes
α Gem	1.58	Ca + Cb	0.814	Torres & Ribas (2002)	
λ Sco	1.62	Aa1 + Aa2	5.925	Tokovinin (2018)	β Cephei variable. Observed by WIRE ¹
β Aur	1.90	Aa + Ab	3.960	Southworth et al. (2007)	Observed by WIRE ² and BRITE ³
δ Vel	1.93	Aa + Ab	45.150	Mérand et al. (2011)	Observed by SMEI ⁴ and BRITE ⁵
β Per	2.09	A + B	2.867	Baron et al. (2012)	Observed by BRITE ⁵
γ And	2.10	Ba + Bb	2.670	Maestre & Wright (1960)	Observed by BRITE ⁵
α CrB	2.22	A + B	17.360	Tomkin & Popper (1986)	See Section 7.2
δ Ori	2.25	Aa1 + Aa2	5.732	Mayer et al. (2010)	Tidally pulsating. Observed by MOST ⁶ and BRITE ⁵

1: Bruntt & Buzasi (2006), 2: Southworth et al. (2007), 3: Strassmeier et al. (2020), 4: Pribulla et al. (2011), 5: Zwintz et al. (2024), 6: Pablo et al. (2015)

systems where individual masses and radii, along with the distance, can be dynamically determined.

8 COMPARISON OF TESS HALO PHOTOMETRY WITH OTHER TELESCOPES

8.1 Comparison with the K2 Bright Star Survey

The stars α Tau (Aldebaran; see Section 4.1), α Vir (Spica), δ Sco (Dschubba), and ζ Sgr (Ascella) are in the K2 Bright Star Survey (Pope et al. 2019b), which also used HALOPHOT. Comparing the HALOPHOT results between this work and K2 Bright Star Survey enables us to test the consistency between the TESS and K2 results and compare the four stars across different instruments.

We downloaded the K2 HALOPHOT light curves from MAST, and de-trended them using the same method as described in Section 3.2. We computed the weighted power spectra, which are shown in Fig. 13 along with the TESS HALOPHOT weighted power spectra.

For Aldebaran and δ Sco, the peaks are not precisely aligned. For Aldebaran, we attribute the non-aligned signal to the star being a

stochastic oscillator. For δ Sco, the non-aligned signal is due to the star being a Be star, which can either have resolved peaks but with variable amplitudes, or the beating of unresolved coherent pulsations can cause time dependency on the light curve. Since both K2 and TESS observed both stars at different times, it is not surprising that the peaks of Aldebaran and δ Sco are not well aligned.

For Spica, the peaks are well aligned in the amplitude spectra, since the star is a coherent variable (ELL + β Cep; Tkachenko et al. 2016). The amplitude from K2 is slightly larger than that from TESS, which may be due to differences between the TESS and Kepler passbands (Lund 2019). The signal is also better resolved in K2 because the star was observed in only one TESS sector (~ 27 d), compared to the one campaign in K2 (~ 80 d).

The star ζ Sgr does not show variability in TESS (in either HALOPHOT or SPOC), but the K2 amplitude spectrum shows a peak around $\sim 2.1 \text{ d}^{-1}$, and the star was listed as a γ Dor variable by Pope et al. (2019b). The K2 light curve for this star contains strong trends, so the claimed γ Dor signal seen in ζ Sgr could be due to instrumental systematics.

We also compared the quality of the light curve using 3, 6, and 12 h Combined Differential Photometric Precision (CDPP; Christiansen

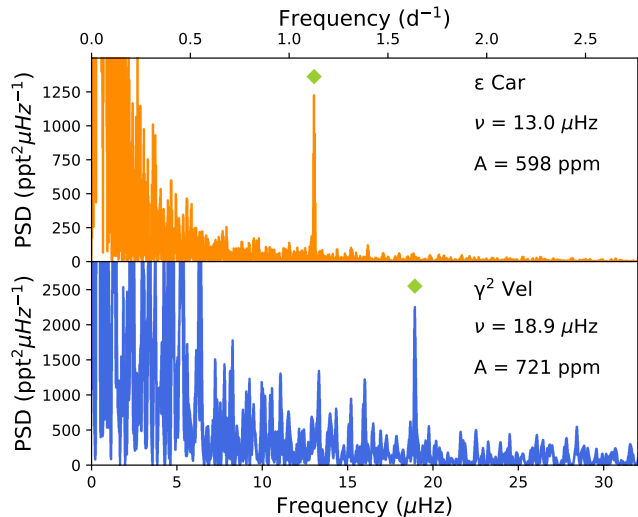


Figure 12. Power density spectra for ϵ Car (top) and γ^2 Vel (bottom). Their pre-whiten frequencies are indicated by the green diamonds, with their corresponding frequencies (ν) and amplitudes (A) shown on the right side of the plot.

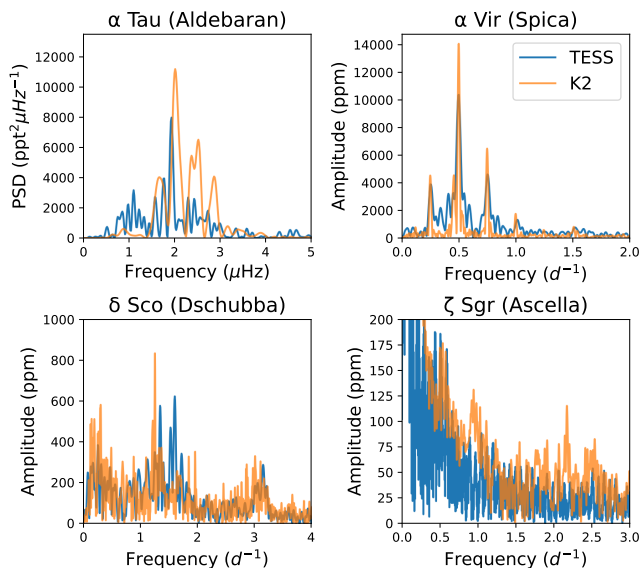


Figure 13. A comparison plot for the power spectrum of the four stars in the *K2* Bright Star Survey. The blue power spectrum is from TESS, while the orange is from *K2*.

et al. 2012) as our proxy for noise. We computed the CDPP using *LIGHTKURVE* for both the TESS and *K2* *HALOPHOT* light curves. For the TESS light curves, we took the mean CDPP for each sector as our comparison value. We show the results in Fig. 14. From the figure, the *HALOPHOT* light curves from *K2* have larger CDPP values, meaning that the noise is generally lower for the TESS data than the *K2* data for this small sample.

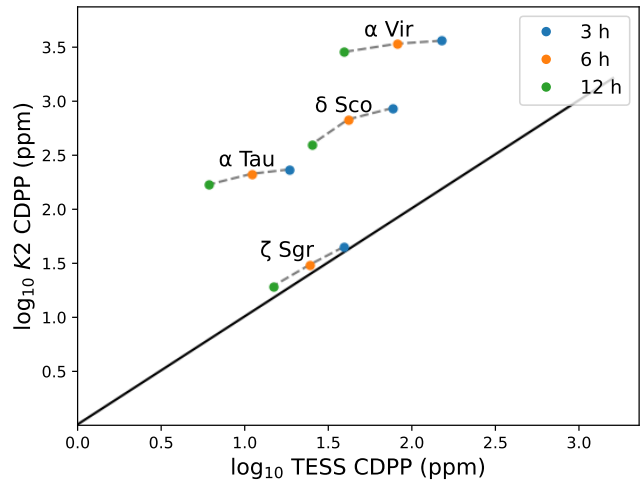


Figure 14. Correlation diagram of the 3, 6, and 12 h *LIGHTKURVE*-computed CDPP for both the TESS and *K2* *HALOPHOT* light curves. Grey dashed lines connect the CDPPs associated with a given star.

8.2 Validity of halo photometry amplitudes with eclipsing binaries

Well-calibrated amplitudes are important for EB studies, and also for simultaneous RV and photometry studies. Therefore, we did a rough analysis in order to test the *HALOPHOT* amplitude. We chose the EBs, β Aur (Menkalinan), β Per (Algol), and α CrB (Alphecca), since they have the best light curves, no significant intrinsic stellar variability, and no long-term trend in their light curves. We calculated the eclipse depth for each sector by subtracting the median flux from the maximum flux, and took the mean of each sector's eclipse depth to obtain the primary eclipse depth for the given star. We compared these values with the eclipse depths reported in the literature, which we estimated from published light curves. We chose light curves obtained with a photometric filter that overlaps the TESS detector's bandpass, which spans 600–1000 nm.

For β Aur, the primary eclipse depth from *HALOPHOT* was 86.6 mmag, which matches with ~ 80 mmag from *BRITE-Toronto*, which has a wavelength range of about 550–700 nm (Strassmeier et al. 2020). Algol has an eclipse depth with *HALOPHOT* of 1059 mmag, which lies between the two eclipse depths of ~ 925 mmag and ~ 1150 mmag from Chen & Reuning (1966), who used filters centred at 1000 nm and 600 nm, respectively. Lastly, α CrB has an eclipse depth with *HALOPHOT* of 114 mmag, which is consistent with the depth of ~ 100 mmag reported by Kron & Gordon (1953) using a filter centred at 723 nm. We also calculated the eclipse depth from the *SPOC* and *QLP* light curves, deriving values of 53 mmag (β Aur), 562 mmag (Algol), and 98 mmag (α CrB)¹¹, which were all much lower than literature values, which we attribute to some (but not all) the saturated pixels being inside the aperture mask (see Section 3.3). The *HALOPHOT* eclipse depths for all three EBs match the literature, giving confidence in the *HALOPHOT* amplitudes.

¹¹ We ignored TESS Sectors 51 and 78 due to the *QLP* light curves containing a lot of noise

9 FUTURE WORK WITH THE TESS HALO PHOTOMETRY SAMPLE

9.1 PLATO

We identified 18 stars in our sample that will be observed by the upcoming PLANetary Transits and Oscillations of stars (PLATO) mission (Rauer et al. 2025), scheduled to launch in early 2027. PLATO has 24 cameras with 25-s cadence, plus two additional fast cameras with 2.5-s cadence that will provide blue (505–700 nm) and red (665–1000 nm) photometry.

The current plan for PLATO is to observe a LOP (Long-duration Observation Phase) field in the south and potentially one LOP field in the north. These LOPs will each cover a $49^\circ \times 49^\circ$ region of the sky, overlapping with the two TESS CVZs and the *Kepler* field (Rauer et al. 2025). PLATO’s current strategy is to observe the southern LOP for two years. Afterwards, it will either continue observing the southern LOP for another two years or shift its field of view to observe the northern LOP for two years. At the time of writing, only the southern LOP (LOPS2), centred around $\alpha = 95.31043$, $\delta = -47.88693$, is defined (Nascimbeni et al. 2025), while for the northern LOP we adopt the candidate field, LOPN1, centred around $\alpha = 277.18023$, $\delta = 52.85952$ (Nascimbeni et al. 2022). In Fig. 15 we show the LOPs in Galactic coordinates, along with the stars in our sample.

The stars in our sample that PLATO could observe are listed in Table 3. Of these, nine will be inside LOPS2, while four stars are within LOPN1. Furthermore, five stars could be within 5° of the two LOPs and so may be observed if the fields are shifted. All of our stars fall outside the dynamic range of the fast cameras ($4 < V < 8$) and the optimised range of the normal cameras ($V \geq 8$), so they will saturate the detector. Furthermore, the stars in our sample do not meet the requirements to be included in the P1, P2, P4, or P5 samples (Montalto et al. 2021; Rauer et al. 2025), but could be included as complementary science targets. Two stars, α Col and γ Dra, might meet the requirements of the Colour Sample, as they could be within the nominal field of view of the fast cameras, allowing imagettes (equivalent to TPFs) to be provided. However, these stars may not be observed because the effective field of view is limited to $\sim 610 \text{ deg}^2$ (Janssen et al. 2024; Rauer et al. 2025) due to the use of frame-transfer CCDs in the fast cameras. For the rest of the sample, it is unclear whether photometry can be performed on board the spacecraft, although halo photometry is being considered for highly saturated stars (Rauer et al. 2025). Our results from TESS can be used to guide the selection of stars for PLATO observations.

9.2 SONG

The Stellar Observations Network Group (SONG) is a network of telescopes dedicated to high-cadence, high-precision ground-based RV observations of solar-like oscillators (Andersen et al. 2014; Grundahl et al. 2017; Lund et al., in prep.). Currently, two SONG nodes are active. One is the 1-m Danish Hertzprung SONG Telescope at Observatorio del Teide in Tenerife (SONG-Tenerife; Grundahl et al. 2017), and the other is at the Mount Kent Observatory near Toowoomba, Queensland, Australia (SONG-Australia; Kjeldsen et al. 2025). Furthermore, while SONG’s primary goal is to obtain high-cadence observations of solar-like oscillators (e.g. Grundahl et al. 2017; Malla et al. 2020; Knudstrup et al. 2023; Kjeldsen et al. 2025), it has also been used for long-term RV monitoring of other intrinsically variable stars (e.g. Spaeth et al. 2025), binaries (e.g. Brogaard et al. 2021; Rudrasingam et al., in prep.), and exoplanet host stars (e.g. Luque et al. 2019; Addison et al. 2021).

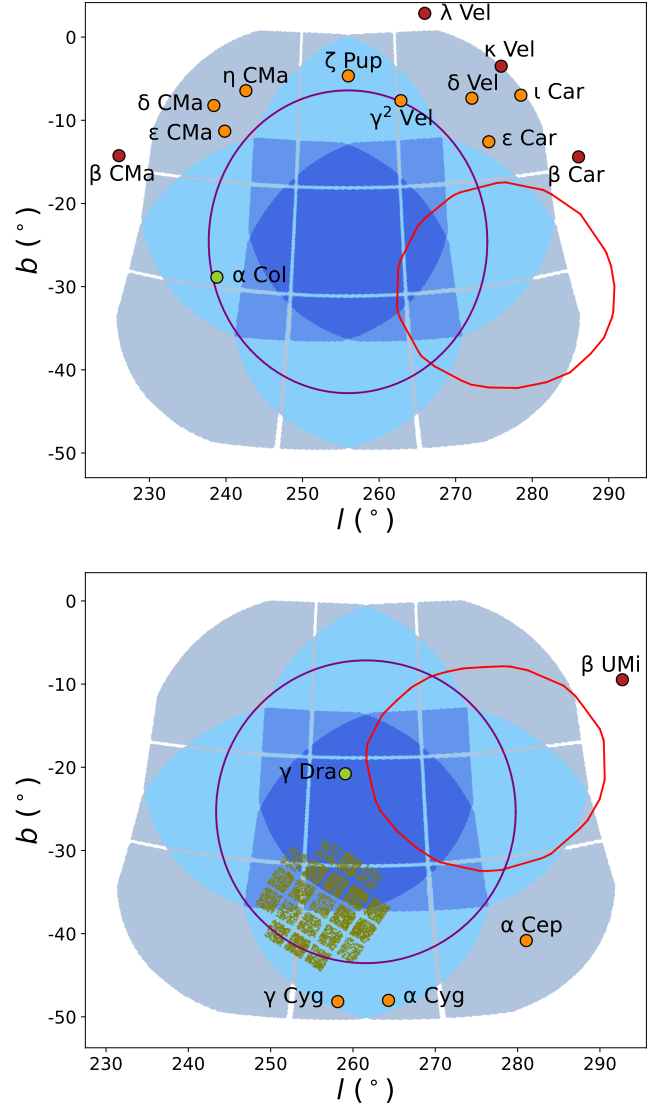


Figure 15. The two PLATO LOPs with the stars in our sample. Top panel shows the PLATO LOPS2 with the southern stars. Bottom panel is the proposed PLATO LOPN1 with the northern stars. In both panels the LOPs are shown blue, with the different shade indicating either 24, 18, 12, or 6 overlapping cameras. The red circles are the TESS CVZs, while the *Kepler* field is shown in olive-green. The field of views of the fast cameras are shown in purple. Orange are stars inside the PLATO LOP, while red are stars within 5° of the LOP. The green are stars inside the field of view of the fast cameras.

We identified 69 stars that have observations from SONG-Tenerife, of which 29 have more than 60 spectra. In Table B1, we list the number of stars in our sample with SONG observations up to and including 2024. We also list 19 stars in Table B2 that have simultaneous TESS and SONG observations. These observations can be used for both forward modelling of stellar variability with simultaneous photometry and RV, thereby removing the stellar signal from RV observations for exoplanet detection (e.g. Beard et al. 2025; Tang et al. 2026). For solar-like oscillators, some of these observations can be used to measure the amplitude ratio and phase difference between photometry and RV (e.g. Jiménez 2002; Huber et al. 2011; Kjeldsen

Table 3. Stars in the PLATO fields

Star	LOP	RA (deg)	DEC (deg)	Sep (deg)	V (mag)	Variability
Inside the fast cameras' field of view						
γ Dra	N1	269.15	51.49	5.11	2.24	RG
α Col	S2	84.91	-34.07	15.85	2.65	Be
Inside PLATO LOPs						
α Cyg	N1	310.36	45.28	22.78	1.25	SLF
ϵ CMa	S2	104.66	-28.97	20.25	1.50	SLF
γ^2 Vel	S2	122.38	-47.34	18.17	1.75	SLF
δ CMa	S2	107.10	-26.39	23.39	1.83	
ϵ Car	S2	125.63	-59.51	21.10	1.86	LPV + SPB/ α^2 CVn
δ Vel	S2	131.18	-54.71	23.15	1.93	EB
ι Car	S2	139.27	-59.28	27.83	2.21	
ζ Pup	S2	120.90	-40.00	19.92	2.21	SLF
γ Cyg	N1	305.56	40.26	22.99	2.23	
η CMa	S2	111.02	-29.30	22.18	2.45	SLF
α Cep	N1	319.64	62.59	24.12	2.45	δ Sct + γ Dor
Near PLATO LOPs						
β Car	S2	138.30	-69.72	154.88	1.67	Var
β CMa	S2	95.67	-17.96	29.93	1.98	β Cep
β UMi	N1	222.68	74.16	145.56	2.07	RG
λ Vel	S2	137.00	-43.43	29.11	2.23	LPV
κ Vel	S2	140.53	-55.01	28.52	2.23	SPB

et al. 2025). The SONG data themselves are hosted on SODA¹², and are freely available upon registration.

10 CONCLUSIONS

We extracted light curves of 98 of the brightest stars observed by TESS in Sectors 1–93 using halo photometry (White et al. 2017; Pope et al. 2019b). We used an updated version of the HALOPHOT, written in the PYTHON framework JAX (Bradbury et al. 2018) framework, to extract the light curves from a 31×31 cut of the Full Frame Images (FFIs) for each star.

We compared the quality of the HALOPHOT light curves with Science Processing Operations Center (SPOC; Jenkins et al. 2016), TESS-SPOC (Caldwell et al. 2020), Quick-look Pipeline (QLP; Huang et al. 2020a,b; Kunimoto et al. 2021, 2022), and non-Total Variation minimised light curves, and found that the HALOPHOT light curves have comparable quality compared to the SPOC light curves, but that the HALOPHOT light curves are of higher quality than SPOC at the bright end of our sample. In contrast, for fainter stars ($V > 2.55$), we observe the opposite trend. A sizeable number of light curves have comparable quality between HALOPHOT and SPOC, but the SPOC light curves had underestimated amplitudes due to aperture masks that included saturated pixels. The QLP light curves are mostly worse than the HALOPHOT light curves.

We detected variability in 15 red giants, and we derived the global asteroseismic parameter, ν_{\max} , using PYMON (Howell et al. 2025) for 13 of them. We then used the derived ν_{\max} and literature radii to estimate their masses. Among the 13 red giants, five of them are

newly discovered solar-like oscillators. For one red giant, β Gem (Pollux), we measured $\Delta\nu$ and derived its seismic mass and radius.

Among the A and early F stars, we detected one γ Doradus variable and five δ Scuti variables, of which two are newly discovered. One of them, α Cep (Alderamin), is a newly discovered δ Scuti– γ Doradus hybrid pulsator. For the O and B stars, we detected nine β Cephei variables, three slowly pulsating B-type stars, eight Be stars, and eight stochastic low-frequency variables. Among them is the binary system ϵ Car (Avior), which we found to be system consisting of a long-period variable and either a slowly pulsating B-type star or a α^2 CVn variable. We also detected eight eclipsing binaries, with one of them, γ And (Almach), being a newly discovered eclipsing binary.

We compared the HALOPHOT results from TESS and K2 for stars in common (Pope et al. 2019b) and found good agreement. We found agreement between the depths of the primary eclipses for three of our EBs with published values.

We identified nine stars that will be inside the PLANetary Transits and Oscillations of stars (PLATO; Rauer et al. 2025) southern Long-duration Observation Phase (LOP) and four that will be inside its northern LOP. Two stars, γ Dra and α Col, will be within the field of view of the fast cameras, potentially enabling multi-colour photometry for both.

Finally, we identified 69 stars in our sample with spectra from the Stellar Observations Network Group (SONG; Andersen et al. 2014; Grundahl et al. 2017; Kjeldsen et al. 2025), of which 29 have more than 60 spectra. Furthermore, 19 stars have simultaneous SONG and TESS observations, enabling forward modelling of stellar variability and, for a few of them, measuring the amplitude ratio and phase difference between photometry and RV.

Altogether, we find 77 out of 98 stars to be variable and provide high-quality HALOPHOT light curves on MAST for easy access and future detailed analysis.

ACKNOWLEDGEMENTS

We are grateful for discussions with Courtney Crawford about the stochastic nature of θ Sco, Jeremy Bailey about stochastic variability in blue supergiants, and Ben Montet about TESS photometry.

We acknowledge and pay respect to the traditional owners of the land on which the University of Sydney and Macquarie University are situated, the Gadigal clan of the Eora Nation and the Wallumattagal clan of the Dharug Nation, upon whose unceded, sovereign, ancestral lands we work. We pay respects to their Ancestors and descendants, who continue cultural and spiritual connections to Country.

JR and TRB have been supported by the Australian Research Council through the Laureate Fellowship FL220100117, BP by the grants DP230101439 and DE210101639, and MGP by the Discovery Early Career Researcher Award (project number DE250100146). We are grateful to the Australian public for enabling this science. MNL acknowledges support from the ESA PRODEX programme (PEA 4000142995).

This paper includes data collected by the TESS mission (Ricker et al. 2015) and K2 mission (Howell et al. 2014). Funding for the TESS and K2 missions is provided by the NASA's Science Mission Directorate. This paper made use of the Hipparcos and Tycho catalogues. Funding for the Hipparcos mission was provided by the European Space Agency. This paper has made use of the SIMBAD¹³

¹² <https://soda.phys.au.dk/>

¹³ <https://simbad.u-strasbg.fr/simbad/sim-basic?ident=m33&submit=SIMBAD+search>

database (Wenger et al. 2000), operated at CDS, Strasbourg, France. This paper has also made use of the SONG database SODA, operated and maintained at Aarhus University, DK.

This research made use of NUMPY (Harris et al. 2020); MATPLOTLIB (Hunter 2007); SCIPY (Virtanen et al. 2020); ASTROPY (Astropy Collaboration et al. 2013, 2018, 2022); ASTROQUERY (Ginsburg et al. 2019); LIGHTKURVE (Lightkurve Collaboration et al. 2018); PANDAS (McKinney 2010); PYMON (Howell et al. 2025); NIFTY-LS (Garrison et al. 2024); UNCERTAINTIES (Lebigot 2023); JAX (Bradbury et al. 2018); and JAXOPT (Blondel et al. 2021).

DATA AVAILABILITY

All codes and data used to produce this work are publicly available and open source. The TESS HALOPHOT module is hosted at <https://github.com/hvidy/halophot> and diagnostic plots are at https://github.com/JonatanRudrasingam/TESS_halophot. All light curves are available from MAST via <https://doi.org/10.17909/tzm7-r151>¹⁴ and accessible under the name “HALO-TESS”.

REFERENCES

- Addison B. C., et al., 2021, *AJ*, **162**, 292
- Aerts C., et al., 2017, *A&A*, **602**, A32
- Aerts C., et al., 2018, *MNRAS*, **476**, 1234
- Al-Naimiy H. M. K., Mutter A. A. A., Flaih H. A., 1985, *Ap&SS*, **108**, 227
- Allende Prieto C., Barklem P. S., Lambert D. L., Cunha K., 2004, *A&A*, **420**, 183
- Andersen M. F., et al., 2014, in *Revista Mexicana de Astronomia y Astrofisica Conference Series*. p. 83 (arXiv:1901.08300, doi:10.48550/arXiv.1901.08300)
- Antoci V., et al., 2014, *ApJ*, **796**, 118
- Antoci V., et al., 2019, *MNRAS*, **490**, 4040
- Arentoft T., et al., 2019, *A&A*, **622**, A190
- Armstrong J. T., et al., 1998, *ApJ*, **496**, 550
- Astropy Collaboration et al., 2013, *A&A*, **558**, A33
- Astropy Collaboration et al., 2018, *AJ*, **156**, 123
- Astropy Collaboration et al., 2022, *ApJ*, **935**, 167
- Aurière M., et al., 2009, *A&A*, **504**, 231
- Aurière M., et al., 2015, *A&A*, **574**, A90
- Aurière M., et al., 2021, *A&A*, **646**, A130
- Avvakumova E. A., Malkov O. Y., Kniazev A. Y., 2013, *Astronomische Nachrichten*, **334**, 860
- Baines E. K., Armstrong J. T., Schmitt H. R., Zavala R. T., Benson J. A., Hutter D. J., Tycner C., van Belle G. T., 2018, *AJ*, **155**, 30
- Baines E. K., et al., 2021, *AJ*, **162**, 198
- Baines E. K., Clark III J. H., Schmitt H. R., Stone J. M., von Braun K., 2023, *AJ*, **166**, 268
- Baines E. K., Clark J. H., Kingsley B. I., Schmitt H. R., Stone J. M., 2025, *AJ*, **169**, 293
- Barac N., Bedding T. R., Murphy S. J., Hey D. R., 2022, *MNRAS*, **516**, 2080
- Barbiano di Belgioioso A., Fracassini M., Pasinetti L. E., Stroppa P., 1983, *Ap&SS*, **94**, 97
- Baron F., et al., 2012, *ApJ*, **752**, 20
- Beard C., et al., 2025, *AJ*, **169**, 92
- Beck P. G., et al., 2020, in Neiner C., Weiss W. W., Baade D., Griffin R. E., Lovekin C. C., Moffat A. F. J., eds, *Stars and their Variability Observed from Space*. pp 75–79 (arXiv:2001.04912, doi:10.48550/arXiv.2001.04912)
- Bedding T. R., Robertson J. G., Marson R. G., 1994, *A&A*, **290**, 340
- Bedding T. R., et al., 2020, *Nature*, **581**, 147
- Begari T., Bernhard K., Paunzen E., Mondal P., 2026, arXiv e-prints, p. arXiv:2601.19782
- Belkacem K., Goupil M. J., Dupret M. A., Samadi R., Baudin F., Noels A., Mosser B., 2011, *A&A*, **530**, A142
- Benbakoura M., et al., 2021, *A&A*, **648**, A113
- Blomme R., et al., 2011, *A&A*, **533**, A4
- Blondel M., Berthet Q., Cuturi M., Frostig R., Hoyer S., Llinares-López F., Pedregosa F., Vert J.-P., 2021, arXiv preprint arXiv:2105.15183
- Bowman D. M., et al., 2019a, *Nature Astronomy*, **3**, 760
- Bowman D. M., et al., 2019b, *A&A*, **621**, A135
- Bowman D. M., Burssens S., Simón-Díaz S., Edelmann P. V. F., Rogers T. M., Horst L., Röpke F. K., Aerts C., 2020, *A&A*, **640**, A36
- Bowman D. M., et al., 2022, *A&A*, **658**, A96
- Bradbury J., et al., 2018, JAX: composable transformations of Python+NumPy programs, <http://github.com/jax-ml/jax>
- Brasseur C. E., Phillip C., Fleming S. W., Mullally S. E., White R. L., 2019, *Astrocute: Tools for creating cutouts of TESS images*, *Astrophysics Source Code Library*, record ascl:1905.007
- Brogaard K., et al., 2021, *A&A*, **645**, A25
- Brogaard K., et al., 2022, *A&A*, **668**, A82
- Brown T. M., Gilliland R. L., Noyes R. W., Ramsey L. W., 1991, *ApJ*, **368**, 599
- Bruntt H., Buzasi D. L., 2006, *Mem. Soc. Astron. Italiana*, **77**, 278
- Buyschaert B., Neiner C., Aerts C., White T. R., Pope B. J. S., 2018, in Di Matteo P., Billebaud F., Herpin F., Lagarde N., Marquette J. B., Robin A., Venot O., eds, *SF2A-2018: Proceedings of the Annual meeting of the French Society of Astronomy and Astrophysics*. p. Di
- Buzasi D., 2000, in Pallavicini R., Micela G., Sciortino S., eds, *Astronomical Society of the Pacific Conference Series Vol. 198, Stellar Clusters and Associations: Convection, Rotation, and Dynamos*. p. 557
- Buzasi D., Catanzarite J., Laher R., Conrow T., Shupe D., Gautier III T. N., Kreidl T., Everett D., 2000, *ApJ*, **532**, L133
- Buzasi D. L., Bruntt H., Preston H. L., Clausen J. V., 2004, in *American Astronomical Society Meeting Abstracts*. p. 18.05
- Buzasi D. L., et al., 2005, *ApJ*, **619**, 1072
- Caldwell D. A., et al., 2020, *Research Notes of the American Astronomical Society*, **4**, 201
- Campante T. L., et al., 2023, *AJ*, **165**, 214
- Campbell W. W., 1900, *ApJ*, **11**, 140
- Carciofi A. C., Okazaki A. T., Le Bouquin J.-B., Štefl S., Rivinius T., Baade D., Bjorkman J. E., Hummel C. A., 2009, *A&A*, **504**, 915
- Chaplin W. J., Miglio A., 2013, *ARA&A*, **51**, 353
- Charbonnel C., et al., 2020, *A&A*, **633**, A34
- Chen K. Y., Reuning E. G., 1966, *AJ*, **71**, 283
- Chontos A., Huber D., Sayeed M., Yamsiri P., 2022, *The Journal of Open Source Software*, **7**, 3331
- Christiansen J. L., et al., 2012, *PASP*, **124**, 1279
- Cohen M., Walker R. G., Carter B., Hammersley P., Kidger M., Noguchi K., 1999, *AJ*, **117**, 1864
- Collins II G. W., 1987, in Slettebak A., Snow T. P., eds, *IAU Colloquium 92: Physics of Be Stars*. p. 3
- Crawford C. L., et al., 2024, *MNRAS*, **528**, 7397
- Crawford C. L., et al., 2025, *MNRAS*, **542**, 3289
- Docobo J. A., Ling J. F., 2007, *AJ*, **133**, 1209
- Dorn-Wallenstein T. Z., Levesque E. M., Davenport J. R. A., 2019, *ApJ*, **878**, 155
- Dupret M.-A., Grigahcène A., Garrido R., Gabriel M., Scuflaire R., 2005, *A&A*, **435**, 927
- Dziembowski W. A., Pamiatnykh A. A., 1993, *MNRAS*, **262**, 204
- Dziembowski W. A., Moskalik P., Pamiatnykh A. A., 1993, *MNRAS*, **265**, 588
- ESA ed. 1997, *The HIPPARCOS and TYCHO catalogues. Astrometric and photometric star catalogues derived from the ESA HIPPARCOS Space Astrometry Mission ESA Special Publication Vol. 1200*
- Eaton J. A., 1975, *PASP*, **87**, 745
- Eaton J. A., Williamson M. H., 2007, *PASP*, **119**, 886
- Eisner N. L., Pope B. J. S., Aigrain S., Barragán O., White T. R., Huang

¹⁴ <https://archive.stsci.edu/hlsp/halo-tess>

- C. X., Lintott C., Volkov A., 2019, *Research Notes of the American Astronomical Society*, 3, 145
- Epanechnikov V. A., 1969, *Theory Probab. Appl*, 14, 153
- Farr W. M., et al., 2018, *ApJ*, 865, L20
- Gaia Collaboration et al., 2023, *A&A*, 674, A1
- Gardner T., et al., 2021, *ApJ*, 921, 41
- Garrison L. H., Foreman-Mackey D., Shih Y.-h., Barnett A., 2024, *Research Notes of the American Astronomical Society*, 8, 250
- Gaulme P., et al., 2016, *ApJ*, 832, 121
- Gaulme P., et al., 2022, *A&A*, 668, A173
- Ginsburg A., et al., 2019, *AJ*, 157, 98
- Girardi L., Bressan A., Bertelli G., Chiosi C., 2000, *A&AS*, 141, 371
- Goodricke J., 1783, *Philosophical Transactions of the Royal Society of London Series I*, 73, 474
- Goupil M. J., Dupret M. A., Samadi R., Boehm T., Alecian E., Suarez J. C., Lebreton Y., Catala C., 2005, *Journal of Astrophysics and Astronomy*, 26, 249
- Gray D. F., 2016, *ApJ*, 832, 68
- Gray D. F., 2018, *ApJ*, 869, 81
- Gray R. O., Garrison R. F., 1989, *ApJS*, 69, 301
- Grundahl F., et al., 2017, *ApJ*, 836, 142
- Guenther D. B., Demarque P., Buzasi D., Catanzarite J., Laher R., Conrow T., Kreidl T., 2000, *ApJ*, 530, L45
- Gutiérrez-Soto J., Fabregat J., Suso J., Lanzara M., Garrido R., Hubert A.-M., Floquet M., 2007, *A&A*, 476, 927
- Guzik J. A., Kaye A. B., Bradley P. A., Cox A. N., Neuforge C., 2000, *ApJ*, 542, L57
- Hanbury Brown R., Davis J., Allen L. R., 1974, *MNRAS*, 167, 121
- Handler G., 2009, in Guzik J. A., Bradley P. A., eds, *American Institute of Physics Conference Series Vol. 1170, Stellar Pulsation: Challenges for Theory and Observation*. AIP, pp 403–409 ([arXiv:2110.09806](https://arxiv.org/abs/2110.09806)), doi:10.1063/1.3246528
- Harris C. R., et al., 2020, *Nature*, 585, 357
- Hatzes A. P., Cochran W. D., 1993, *ApJ*, 413, 339
- Hatzes A. P., Cochran W. D., 1998a, in Donahue R. A., Bookbinder J. A., eds, *Astronomical Society of the Pacific Conference Series Vol. 154, Cool Stars, Stellar Systems, and the Sun*. p. 311
- Hatzes A. P., Cochran W. D., 1998b, *MNRAS*, 293, 469
- Hatzes A. P., Zechmeister M., 2007, *ApJ*, 670, L37
- Hatzes A. P., et al., 2006, *A&A*, 457, 335
- Hatzes A. P., et al., 2012, *A&A*, 543, A98
- Hatzes A. P., et al., 2015, *A&A*, 580, A31
- Hatzes A. P., et al., 2018, *AJ*, 155, 120
- Hauck B., 1971, *A&A*, 11, 79
- Hernandez C. A., Sahade J., 1980, *PASP*, 92, 819
- Higl J., Weiss A., 2017, *A&A*, 608, A62
- Hill M. L., et al., 2021, *AJ*, 162, 211
- Hinkley S., et al., 2011, *ApJ*, 726, 104
- Hoffleit D., Warren Jr. W. H., 1995, *VizieR Online Data Catalog: Bright Star Catalogue, 5th Revised Ed. (Hoffleit+, 1991), VizieR Online Data Catalog: V/50*. Originally published in: 1964BS....C.....0H; 1991bsc.book.....H
- Høg E., et al., 1997, *A&A*, 323, L57
- Hogg D. W., Foreman-Mackey D., 2014, *OWL*, github, <https://github.com/davidwhogg/OWL/>
- Holdsworth D. L., et al., 2021, *MNRAS*, 506, 1073
- Hon M., et al., 2021, *ApJ*, 919, 131
- Howell S. B., et al., 2014, *PASP*, 126, 398
- Howell M., Campbell S. W., Kalup C., Stello D., De Silva G. M., 2025, *MNRAS*, 536, 1389
- Huang C. X., et al., 2020a, *Research Notes of the American Astronomical Society*, 4, 204
- Huang C. X., et al., 2020b, *Research Notes of the American Astronomical Society*, 4, 206
- Huber D., Stello D., Bedding T. R., Chaplin W. J., Arentoft T., Quirion P.-O., Kjeldsen H., 2009, *Communications in Asteroseismology*, 160, 74
- Huber D., et al., 2011, *ApJ*, 731, 94
- Hunter J. D., 2007, *Computing in Science & Engineering*, 9, 90
- Jackson B. V., et al., 2004, *Sol. Phys.*, 225, 177
- Jancart S., Jorissen A., Babusiaux C., Pourbaix D., 2005, *A&A*, 442, 365
- Jannsen N., et al., 2024, *A&A*, 681, A18
- Jenkins J. M., et al., 2016, in Chiozzi G., Guzman J. C., eds, *Society of Photo-Optical Instrumentation Engineers (SPIE) Conference Series Vol. 9913, Software and Cyberinfrastructure for Astronomy IV*. p. 99133E, doi:10.1117/12.2233418
- Jiménez A., 2002, *ApJ*, 581, 736
- Kallinger T., et al., 2010, *A&A*, 509, A77
- Kallinger T., et al., 2019, *A&A*, 624, A35
- Keenan P. C., McNeil R. C., 1989, *ApJS*, 71, 245
- Kim H.-I., 1989, *ApJ*, 342, 1061
- Kim K. M., Mkrtichian D. E., Lee B.-C., Han I., Hatzes A. P., 2006, *A&A*, 454, 839
- Kjeldsen H., Bedding T. R., 1995, *A&A*, 293, 87
- Kjeldsen H., et al., 2025, *A&A*, 700, A39
- Knudstrup E., et al., 2023, *A&A*, 675, A197
- Kourniotis M., Cidale L. S., Kraus M., Ruiz Diaz M. A., Alberici Adam A., 2025, *A&A*, 697, A152
- Kron G. E., Gordon K. C., 1953, *ApJ*, 118, 55
- Kunimoto M., et al., 2021, *Research Notes of the American Astronomical Society*, 5, 234
- Kunimoto M., Tey E., Fong W., Hesse K., Shporer A., Fausnaugh M., Vanderpek R., Ricker G., 2022, *Research Notes of the American Astronomical Society*, 6, 236
- Kurtz D. W., 1990, *ARA&A*, 28, 607
- Labadie-Bartz J., et al., 2017, *AJ*, 153, 252
- Labadie-Bartz J., Carciofi A. C., Henrique de Amorim T., Rubio A., Luiz Figueiredo A., Ticiani dos Santos P., Thomson-Paressant K., 2022, *AJ*, 163, 226
- Le Dizès C., Rieutord M., Charpinet S., 2021, *A&A*, 653, A26
- Lebigot E. O., 2023, *Uncertainties: a Python package for calculations with uncertainties*, <http://pythonhosted.org/uncertainties/>
- Lenoir-Craig G., et al., 2022, *ApJ*, 925, 79
- Lewis F., Bailey J., Cotton D. V., Howarth I. D., Kedziora-Chudczer L., van Leeuwen F., 2022, *MNRAS*, 513, 1129
- Li T., Bedding T. R., Huber D., Ball W. H., Stello D., Murphy S. J., Bland-Hawthorn J., 2018, *MNRAS*, 475, 981
- Li Y., et al., 2023, *MNRAS*, 523, 916
- Lightkurve Collaboration et al., 2018, *Lightkurve: Kepler and TESS time series analysis in Python, Astrophysics Source Code Library, record ascl:1812.013 (ascl:1812.013)*
- Lomb N. R., 1976, *Ap&SS*, 39, 447
- Longmore A. J., Jameson R. F., 1975, *MNRAS*, 173, 271
- Lund M. N., 2019, *MNRAS*, 489, 1072
- Lund M. N., et al., 2025, *A&A*, 701, A285
- Luque R., et al., 2019, *A&A*, 631, A136
- Maestre L. A., Wright J. A., 1960, *ApJ*, 131, 119
- Malkov O. Y., Oblak E., Snegireva E. A., Torra J., 2006, *A&A*, 446, 785
- Malla S. P., et al., 2020, *MNRAS*, 496, 5423
- Massarotti A., Latham D. W., Stefanik R. P., Fogel J., 2008, *AJ*, 135, 209
- Mayer P., Harmanec P., Wolf M., Božić H., Šlechta M., 2010, *A&A*, 520, A89
- McKinney W., 2010, in van der Walt S., Millman J., eds, *Proceedings of the 9th Python in Science Conference*. pp 56–61, doi:10.25080/Majora-92bf1922-00a
- Mérand A., et al., 2011, *A&A*, 532, A50
- Millis R. L., 1966, *PASP*, 78, 340
- Monnier J. D., Townsend R. H. D., Che X., Zhao M., Kallinger T., Matthews J., Moffat A. F. J., 2010, *ApJ*, 725, 1192
- Montalto M., et al., 2021, *A&A*, 653, A98
- Montanari G., 1671, in Capponi G. B., ed., *Prose de' signori Accademici Gelati di Bologna*. Bologna: Manolessi, pp 369–392
- Nascimbeni V., et al., 2022, *A&A*, 658, A31
- Nascimbeni V., et al., 2025, *A&A*, 694, A313
- Otoni G., et al., 2022, *A&A*, 657, A187
- Pablo H., et al., 2015, *ApJ*, 809, 134
- Pablo H., et al., 2016, *PASP*, 128, 125001

- Paegert M., Stassun K. G., Collins K. A., Pepper J., Torres G., Jenkins J., Twicken J. D., Latham D. W., 2022, *VizieR Online Data Catalog: TESS Input Catalog version 8.2 (TIC v8.2)* (Paegert+, 2021), *VizieR On-line Data Catalog: IV/39*. Originally published in: 2021arXiv210804778P
- Parsons S. B., Ake T. B., 1998, *ApJS*, **119**, 83
- Pedersen M. G., Bildsten L., 2025, *MNRAS*, **539**, 2742
- Pedersen M. G., et al., 2019, *ApJ*, **872**, L9
- Perryman M. A. C., et al., 1997, *A&A*, **323**, L49
- Plummer H. C., 1908, *Lick Observatory Bulletin*, **5**, 24
- Pope B. J. S., et al., 2016, *MNRAS*, **455**, L36
- Pope B. J. S., et al., 2019a, *ApJS*, **244**, 18
- Pope B. J. S., et al., 2019b, *ApJS*, **245**, 8
- Pribulla T., et al., 2011, *A&A*, **528**, A21
- Ramirez Delgado V., Dodson-Robinson S., 2020, *Research Notes of the American Astronomical Society*, **4**, 153
- Rauer H., et al., 2025, *Experimental Astronomy*, **59**, 26
- Reffert S., Quirrenbach A., Mitchell D. S., Albrecht S., Hekker S., Fischer D. A., Marcy G. W., Butler R. P., 2006, *ApJ*, **652**, 661
- Reffert S., Bergmann C., Quirrenbach A., Trifonov T., Künstler A., 2015, *A&A*, **574**, A116
- Reichert K., Reffert S., Stock S., Trifonov T., Quirrenbach A., 2019, *A&A*, **625**, A22
- Retter A., Bedding T. R., Buzasi D. L., Kjeldsen H., Kiss L. L., 2004, *ApJ*, **601**, L95
- Richardson N. D., et al., 2017, *MNRAS*, **471**, 2715
- Ricker G. R., et al., 2014, in Oschmann Jr. J. M., Clampin M., Fazio G. G., MacEwen H. A., eds, *Society of Photo-Optical Instrumentation Engineers (SPIE) Conference Series Vol. 9143, Space Telescopes and Instrumentation 2014: Optical, Infrared, and Millimeter Wave*. p. 914320 ([arXiv:1406.0151](https://arxiv.org/abs/1406.0151)), [doi:10.1117/12.2063489](https://doi.org/10.1117/12.2063489)
- Ricker G. R., et al., 2015, *Journal of Astronomical Telescopes, Instruments, and Systems*, **1**, 014003
- Rieutord M., Reese D. R., Mombarg J. S. G., Charpinet S., 2024, *A&A*, **687**, A259
- Rivinius T., Klement R., 2026, in *Encyclopedia of Astrophysics*. pp 430–448 ([arXiv:2411.06882](https://arxiv.org/abs/2411.06882)), [doi:10.1016/B978-0-443-21439-4.00042-0](https://doi.org/10.1016/B978-0-443-21439-4.00042-0)
- Rivinius T., Carciofi A. C., Martayan C., 2013, *A&ARv*, **21**, 69
- Roberts D. H., Lehar J., Dreher J. W., 1987, *AJ*, **93**, 968
- Samus' N. N., Kazarovets E. V., Durlevich O. V., Kireeva N. N., Pastukhova E. N., 2017, *Astronomy Reports*, **61**, 80
- Scargle J. D., 1982, *ApJ*, **263**, 835
- Schimak L. S., et al., 2026, *MNRAS*, **546**, [stag151](https://arxiv.org/abs/2601.1511)
- Schmutz W., et al., 1997, *A&A*, **328**, 219
- Sharma S., Stello D., Bland-Hawthorn J., Huber D., Bedding T. R., 2016, *ApJ*, **822**, 15
- Sharma A. N., Bedding T. R., Saio H., White T. R., 2022, *MNRAS*, **515**, 828
- Smyth M. J., Dow M. J., Napier W. M., 1975, *MNRAS*, **172**, 235
- Southworth J., Bowman D., 2025, *arXiv e-prints*, p. [arXiv:2509.08426](https://arxiv.org/abs/2509.08426)
- Southworth J., Bruntt H., Buzasi D. L., 2007, *A&A*, **467**, 1215
- Spaeth D., et al., 2025, *A&A*, **697**, A32
- Stebbins J., 1910, *ApJ*, **32**, 185
- Stello D., Bruntt H., Preston H., Buzasi D., 2008, *ApJ*, **674**, L53
- Strassmeier K. G., Ilyin I., Weber M., 2018, *A&A*, **612**, A45
- Strassmeier K. G., et al., 2020, *A&A*, **644**, A104
- Struve O., 1931, *ApJ*, **73**, 94
- Tang J., et al., 2026, *AJ*, **171**, 123
- Tarrant N. J., Chaplin W. J., Elsworth Y., Spreckley S. A., Stevens I. R., 2008, *A&A*, **483**, L43
- Telting J. H., Schrijvers C., Ilyin I. V., Uytterhoeven K., De Ridder J., Aerts C., Henrichs H. F., 2006, *A&A*, **452**, 945
- Thomsen J. S., et al., 2025, *A&A*, **699**, A152
- Thoul A., 2009, *Communications in Asteroseismology*, **159**, 35
- Tkachenko A., et al., 2016, *MNRAS*, **458**, 1964
- Tokovinin A., 2018, *ApJS*, **235**, 6
- Tomkin J., Popper D. M., 1986, *AJ*, **91**, 1428
- Torres G., Ribas I., 2002, *ApJ*, **567**, 1140
- Ulrich R. K., 1986, *ApJ*, **306**, L37
- Videla M., Mendez R. A., Clavería R. M., Silva J. F., Orchard M. E., 2022, *AJ*, **163**, 220
- Virtanen P., et al., 2020, *Nature Medicine*, **17**, 261
- Vogel H. C., 1890, *Astronomische Nachrichten*, **123**, 289
- Walker G., et al., 2003, *PASP*, **115**, 1023
- Watson C., Henden A. A., Price A., 2016, *VizieR Online Data Catalog: AAVSO International Variable Star Index VSX (Watson+, 2006-2014)*, *VizieR On-line Data Catalog: B/vsx*. Originally published in: 2006SASS...25...47W
- Weiss W. W., et al., 2014, *PASP*, **126**, 573
- Wenger M., et al., 2000, *A&AS*, **143**, 9
- White T. R., et al., 2017, *MNRAS*, **471**, 2882
- Winn J. N., 2024, p. [arXiv:2410.12905](https://arxiv.org/abs/2410.12905) ([arXiv:2410.12905](https://arxiv.org/abs/2410.12905)), [doi:10.48550/arXiv.2410.12905](https://doi.org/10.48550/arXiv.2410.12905)
- Yu J., Huber D., Bedding T. R., Stello D., Hon M., Murphy S. J., Khanna S., 2018, *ApJS*, **236**, 42
- Yu J., Bedding T. R., Stello D., Huber D., Compton D. L., Gizon L., Hekker S., 2020, *MNRAS*, **493**, 1388
- Zeilik M., Bayliss L., Heckert P., 1980, *Information Bulletin on Variable Stars*, **1787**, 1
- Zhang Z., Ren Y., Jiang B., Soszyński I., Jayasinghe T., 2024, *ApJ*, **969**, 81
- Zwintz K., et al., 2020, *A&A*, **643**, A110
- Zwintz K., et al., 2024, *A&A*, **683**, A49
- van Belle G. T., et al., 2006, *ApJ*, **637**, 494
- van Leeuwen F., Evans D. W., Grenon M., Grossmann V., Mignard F., Perryman M. A. C., 1997, *A&A*, **323**, L61

APPENDIX A: LIST OF STARS

Table A1: All TESS stars with Halo Photometry.

Star	Name	TIC	HD	V	$B - V$	M_V	Spectral type	N	N_H	N_P	Variability
α Eri	Achernar	230981971	10144	0.45	-0.16	-2.77	B3Vpe	3	3	1	Be
α Ori	Betelgeuse	269273552	39801	0.45	1.50	-5.14	M1-2Ia-Iab	3	0	0	
β Cen	Hadar	328329822	122451	0.61	-0.23	-5.42	B1III	3	3	1	β Cep
α Aql	Altair	70257116	187642	0.76	0.22	2.20	A7V	2	2	0	δ Sct
α Cru	Acrux	450568754	108248	0.77	-0.24	-4.19	B0.5IV+B1V	4	4	0	β Cep
α Tau	Aldebaran	245873777	29139	0.87	1.54	-0.63	K5+III	4	4	0	RG
α Vir	Spica	178999156	116658	0.98	-0.23	-3.55	B1III-IV+B2V	1	1	0	β Cep + ELL
α Sco	Antares	175934060	148478	1.06	1.87	-5.28	M1.5Iab-Ib+B4Ve	1	0	0	
β Gem	Pollux	423088367	62509	1.16	0.99	1.09	K0IIIb	5	5	0	RG
α PsA	Fomalhaut	47552789	216956	1.17	0.14	1.74	A3V	3	0	0	
α Cyg	Deneb	195554360	197345	1.25	0.09	-8.73	A2Ia	6	6	0	SLF
β Cru	Mimosa	405567821	111123	1.25	-0.24	-3.92	B0.5III	5	4	5	β Cep
α Leo	Regulus	357348164	87901	1.36	-0.09	-0.52	B7V	1	0	0	
ϵ CMa	Adhara	63198307	52089	1.50	-0.21	-4.10	B2II	5	5	5	SLF
α Gem	Castor	239187696	60179	1.58	0.03	0.59	A2Vm+A1V	8	6	8	EB
γ Cru	Gacrux	272314138	108903	1.59	1.60	-0.56	M3.5III	4	4	0	LPV
λ Sco	Shaula	465088681	158926	1.62	-0.23	-5.05	B2IV+B	4	2	3	β Cep + EB
γ Ori	Bellatrix	365572007	35468	1.64	-0.22	-2.72	B2III	2	2	0	Var
β Tau	Elnath	285473140	35497	1.65	-0.13	-1.37	B7III	4	0	4	α^2 CVn
β Car	Miaplacidus	290374453	80007	1.67	0.07	-0.99	A2IV	10	0	5	Var
ϵ Ori	Alnilam	427451176	37128	1.69	-0.18	-6.38	B0Ia	2	2	2	SLF
α Gru	Alnair	279316667	209952	1.73	-0.07	-0.73	B7IV	2	0	0	
ζ Ori	Alnitak	11360636	37742	1.74	-0.20	-5.26	O9.7Ib+B0III	1	1	1	SLF
γ^2 Vel		354825513	68273	1.75	-0.14	-5.31	WC8+O9I	8	7	8	SLF
ϵ UMa	Alioth	150387644	112185	1.76	-0.02	-0.21	A0pCr	6	6	0	α^2 CVn
ϵ Sgr	Kaus Australis	66389641	169022	1.79	-0.03	-1.44	B9.5III	5	4	1	Rot
α Per	Mirfak	252830952	20902	1.79	0.48	-4.50	F5Ib	3	0	0	
α UMa	Dubhe	99843265	95689	1.81	1.06	-1.08	K0IIIa	4	4	0	RG
δ CMa	Wezen	64602863	54605	1.83	0.67	-6.87	F8Ia	5	0	0	
η UMa	Alkaid	219033887	120315	1.85	-0.10	-0.60	B3V	5	5	5	Be
θ Sco	Sargas	17158018	159532	1.86	0.41	-2.75	F1II	2	2	0	SLF?
ϵ Car	Avior	342884451	71129	1.86	1.20	-4.58	K3III+B2:V	12	12	0	LPV + SPB/ α^2 CVn
β Aur	Menkalinan	440388263	40183	1.90	0.08	-0.10	A2IV	3	3	0	EB
α TrA	Atria	364216056	150798	1.91	1.45	-3.62	K2IIb-IIIa	3	3	1	LPV
γ Gem	Alhena	308056612	47105	1.93	0.00	-0.60	A0IV	7	0	0	
δ Vel	Alsephina	45696212	74956	1.93	0.04	-0.01	A1V	5	4	0	EB
α Pav	Peacock	219974785	193924	1.94	-0.12	-1.81	B2IV	3	3	0	SPB
α UMi	Polaris	303256075	8890	1.97	0.64	-3.64	F7:Ib-II	14	14	3	Cepheid
β CMa	Mirzam	34590771	44743	1.98	-0.24	-3.95	B1II-III	3	3	1	β Cep
α Hya	Alphard	46799297	81797	1.99	1.44	-1.69	K3II-III	4	4	0	LPV
γ Leo	Algieba	95431294	89484	2.01	1.13	-0.92	G7IIIFe-1+K1-IIIbFe-0.5	4	4	0	RG
α Ari	Hamal	306349516	12929	2.01	1.15	0.48	K2-IIIcA-1	6	5	0	RG
β Cet	Diphda	114434141	4128	2.04	1.02	-0.30	G9.5IIICH-1	2	0	0	
σ Sgr	Nunki	91093307	175191	2.05	-0.13	-2.14	B2.5V	1	1	1	SPB
θ Cen	Menkent	179323446	123139	2.06	1.01	0.70	K0-IIIb	3	3	0	RG
β And	Mirach	174500619	6860	2.07	1.58	-1.86	M0+IIIa	3	3	0	LPV
β UMi	Kochab	229540730	131873	2.07	1.47	-0.87	K4-III	16	16	0	RG
κ Ori	Saiph	66651575	38771	2.07	-0.17	-4.65	B0.5I	2	2	0	SLF
α And	Alpheratz	427733653	358	2.07	-0.04	-0.30	B8IVpMnHg	3	3	2	α^2 CVn
β Gru	Tiaki	44577667	214952	2.07	1.61	-1.52	M5III	3	3	0	LPV
α Oph	Rasalhague	289643770	159561	2.08	0.16	1.30	A5III	1	1	0	δ Sct + γ Dor
β Per	Algol	346783960	193565	2.09	-0.00	-0.18	B8V	3	3	0	EB
γ And	Almach	292057658	12533	2.10	1.37	-3.08	K3-IIb	3	3	0	EB
β Leo	Denebola	14725877	102647	2.14	0.09	1.92	A3V	3	0	0	
γ Cas		51962733	5394	2.15	-0.05	-4.22	B0IVe	6	6	6	Be
γ Cen	Muhlifain	161739042	110304	2.20	-0.02	-0.81	A1IV	4	4	4	Rot

ζ Pup	Naos	133422778	66811	2.21	-0.27	-5.95	O5f	8	7	8	SLF
ι Car	Aspidiske	386296645	80404	2.21	0.19	-4.42	A8Ib	9	0	0	
α CrB	Alphecca	274945059	139006	2.22	0.03	0.42	A0V+G5V	3	3	0	EB
γ Cyg	Sadr	13431346	194093	2.23	0.67	-6.12	F8Ib	7	0	0	
ζ UMa	Mizar	159190005	116656	2.23	0.06	0.33	A1m + A1VpSrSi	5	0	0	
λ Vel	Suhail	31975064	78647	2.23	1.66	-3.99	K4.5Ib-II	6	6	0	LPV
γ Dra	Eltanin	329269366	164058	2.24	1.52	-1.04	K5III	18	18	0	RG
α Cas	Schedar	312141546	3712	2.24	1.17	-1.99	K0IIIa	5	5	1	RG
δ Ori	Mintaka	50743469	36485	2.25	-0.17	-4.99	O9.5II	2	2	0	EB
β Cas	Caph	396298498	432	2.28	0.38	1.17	F2III-IV	9	9	8	δ Sct
ϵ Cen		241398115	118716	2.29	-0.17	-3.02	B1III	3	3	0	β Cep
ϵ Sco	Larawag	191437754	151680	2.29	1.14	0.78	K2.5III	3	3	0	RG
δ Sco	Dschubba	12725034	143275	2.29	-0.12	-3.16	B0.3IV	1	1	1	Be
α Lup	Uridim	129117325	129056	2.30	-0.15	-3.83	B1.5III/Vn	3	3	1	β Cep
η Cen		128116539	127972	2.33	-0.16	-2.55	B1.5Vne	3	2	2	Be
β UMa	Merak	141120277	95418	2.34	0.03	0.41	A1V	3	0	0	
ϵ Boo	Izar	219827143	129988	2.35	0.97	-1.69	K0-II-III	3	3	0	RG
ϵ Peg	Enif	466337046	206778	2.38	1.52	-4.19	K2Ib	2	0	0	
κ Sco	Girtab	147868882	160578	2.39	-0.17	-3.38	B1.5III	3	0	3	β Cep
α Phe	Ankaa	80256524	2261	2.40	1.08	0.52	K0III	2	2	1	RG
γ UMa	Phecda	11895653	103287	2.41	0.04	0.36	A0Ve	5	0	0	
η Oph	Sabik	400036304	155125	2.43	0.06	0.37	A2V	1	0	0	
β Peg	Scheat	436774002	217906	2.44	1.65	-1.49	M2.5II-III	2	2	0	LPV
α Cep	Alderamin	417604820	203280	2.45	0.26	1.58	A7V	11	11	2	δ Sct + γ Dor
η CMa	Aludra	107415639	58350	2.45	-0.08	-7.51	B5Ia	4	4	0	SLF
κ Vel	Markeb	387106852	81188	2.47	-0.14	-3.62	B2IV-V	6	6	0	SPB
ϵ Cyg	Aljanah	232853959	197989	2.48	1.02	0.76	K0-III	5	5	0	RG
ζ Oph		152859121	149757	2.54	0.04	-3.20	O9.5Vn	1	1	0	Be
ζ Cen	Leepwal	113350416	121263	2.55	-0.18	-2.81	B2.5IV	3	3	0	Heartbeat star
δ Leo	Zosma	159523958	97603	2.56	0.13	1.32	A4V	2	2	2	Rot
γ Crv	Gienah	348987372	106625	2.58	-0.11	-0.94	B8IIpHgMn	4	1	3	Rot
δ Cen		333670784	105435	2.58	-0.13	-2.84	B2IVne	3	2	3	Be
α Lep	Arneb	46312112	36673	2.58	0.21	-5.40	F0Ib	1	0	0	
ζ Sgr	Ascella	30504485	176687	2.60	0.06	0.42	A2III+A4IV	3	0	0	
β Lib	Zubeneschamali	79391147	135742	2.61	-0.07	-0.84	B8V	2	0	0	
α Ser	Unukalhai	296856546	140573	2.63	1.17	0.87	K2IIIbCN1	1	1	1	RG
β Ari	Sheratan	91356756	11636	2.64	0.17	1.33	A5V	5	0	5	γ Dor
β Crv	Kraz	83151778	109379	2.65	0.89	-0.51	G5II	1	0	0	
α Col	Phact	140214221	37795	2.65	-0.12	-1.93	B7IVe	5	0	5	Be
θ Aur	Mahasim	174671483	40312	2.65	-0.08	-0.98	A0pSi	2	2	1	α^2 CVn
δ Cas	Ruchbah	54995745	8538	2.66	0.16	0.24	A5III-IV	3	1	3	δ Sct
β Her	Kornephoros	284853659	148856	2.78	0.95	-0.50	G7IIIa	5	5	0	RG

APPENDIX B: STARS WITH SONG OBSERVATIONS

Here we list the stars with SONG observations. In the first table (Table B1), we list the star, HIP number, apparent magnitude in V , the number of spectra, and our TESS variability classification. In the second table (Table B2), we list the stars that have simultaneous SONG and TESS observations. Here we show the star, HIP number, number of simultaneous observations, median time difference in minutes, the Nyquist frequency in μHz , and our TESS variability classification. The SONG observations were obtained from SODA, and includes all observations up to and including 2024.

Table B1: Stars with SONG observation

Star	HIP	V	N_{spectra}	Variability
θ Cen	68933	2.06	7669	RG
β Gem	37826	1.16	7609	RG
ϵ Ori	26311	1.69	5583	SLF
ϵ Cyg	102488	2.48	5359	RG
λ Sco	85927	1.62	4296	β Cep + EB
α Tau	21421	0.87	3234	RG
α Ori	27989	0.45	1331	LPV
β Per	14576	2.09	1237	EB
κ Ori	27366	2.07	1196	SLF
δ Ori	25930	2.25	1094	EB
β Cas	746	2.28	770	δ Sct
α Ari	9884	2.01	761	RG
θ Aur	28380	2.65	707	α^2 CVn
α UMi	11767	1.97	634	Cepheid
β Aur	28360	1.90	619	EB
γ Dra	87833	2.24	590	RG
γ Leo	50583	2.01	574	RG
α Sco	80763	1.06	545	LPV
β UMi	72607	2.07	486	RG
ϵ Boo	72105	2.35	463	RG
α UMa	54061	1.81	428	RG
α Leo	49669	1.36	365	
α CrB	76267	2.22	323	EB
α Hya	46390	1.99	307	LPV
ζ UMa	65378	2.23	283	
γ Cas	4427	2.15	233	Be
η UMa	67301	1.85	203	Be
α And	677	2.07	88	α^2 CVn
γ Cyg	100453	2.23	61	
α Cas	3179	2.24	6	RG
ζ Oph	81377	2.54	6	Be
β Leo	57632	2.14	6	
δ Leo	54872	2.56	6	Rot
α Oph	86032	2.08	6	δ Sct + γ Dor
α Cyg	102098	1.25	5	SLF
γ Gem	31681	1.93	4	
β And	5447	2.07	4	LPV
η CMa	35904	2.45	4	SLF
δ Cas	6686	2.66	3	δ Sct
γ Crv	59803	2.58	3	Rot
α Aql	97649	0.76	3	δ Sct
β Crv	61359	2.65	3	
α Vir	65474	0.98	3	β Cep + ELL
β Ari	8903	2.64	3	γ Dor
α Ser	77070	2.63	3	RG
α PsA	113368	1.17	3	
β Lib	74785	2.61	3	
ζ Sgr	93506	2.60	3	
ϵ CMa	33579	1.50	3	SLF
α Gem	36850	1.58	3	EB
α Lep	25985	2.58	3	

γ Ori	25336	1.64	3	Var
β Tau	25428	1.65	3	Rot
ζ Ori	26727	1.74	3	SLF
γ And	9640	2.10	3	EB
ϵ UMa	62956	1.76	3	α^2 CVn
α Per	15863	1.79	3	
δ CMa	34444	1.83	3	
α Cep	105199	2.45	3	δ Sct + γ Dor
β Peg	113881	2.44	3	LPV
η Oph	84012	2.43	3	
γ UMa	58001	2.41	3	
β CMa	30324	1.98	3	β Cep
ϵ Peg	107315	2.38	3	LPV
β UMa	53910	2.34	3	
δ Sco	78401	2.29	3	Be
β Cet	3419	2.04	3	
σ Sgr	92855	2.05	3	SPB
β Her	80816	2.78	3	RG

Table B2: Simultaneous TESS and SONG stars

Star	HIP	Simultaneous	Δt (min)	ν_{Nyquist} (μHz)	Variability
θ Cen	68933	5419	1.088	7659.314	RG
β Gem	37826	68	0.812	10262.726	RG
ϵ Cyg	102488	2	1031980.025	0.008	RG
λ Sco	85927	1181	6.088	1368.813	β Cep + EB
α Tau	21421	153	0.68	12254.902	RG
β Per	14576	7	1903.868	4.377	EB
α Ari	9884	98	1.845	4516.712	RG
α UMi	11767	324	2.114	3941.974	Cepheid
β Aur	28360	58	29.81	279.548	EB
γ Dra	87833	112	1755.446	4.747	RG
γ Leo	50583	23	2917.931	2.856	RG
β UMi	72607	198	0.63	13227.513	RG
ϵ Boo	72105	48	1413.474	5.896	RG
α UMa	54061	3	1436.742	5.8	RG
α CrB	76267	18	85.955	96.95	EB
α Hya	46390	36	258.096	32.288	LPV
ζ UMa	65378	27	1479.122	5.634	
η UMa	67301	29	1.09	7645.26	Be
γ Cyg	100453	8	7390.715	1.128	

This paper has been typeset from a $\text{\TeX}/\text{\LaTeX}$ file prepared by the author.